Gold-Induced Nanostructuring of Silicon Surfaces

By

Laura Pedri

A thesis submitted in partial fulfillment of the requirements for the degree of M.Sc. in Physics at Lakehead University

August 2005

Reproduced with permission of the copyright owner. Further reproduction prohibited without permission.

Library and Archives Canada

Published Heritage Branch

395 Wellington Street
Ottawa ON K1A 0N4
Canada

Bibliothèque et Archives Canada

Direction du Patrimoine de l'édition

395, rue Wellington
Ottawa ON K1A 0N4
Canada

Your file Votre référence
ISBN: 978-0-494-15638-4
Our file Notre référence
ISBN: 978-0-494-15638-4

NOTICE:
The author has granted a non-exclusive license allowing Library and Archives Canada to reproduce, publish, archive, preserve, conserve, communicate to the public by telecommunication or on the Internet, loan, distribute and sell theses worldwide, for commercial or non-commercial purposes, in microform, paper, electronic and/or any other formats.

The author retains copyright ownership and moral rights in this thesis. Neither the thesis nor substantial extracts from it may be printed or otherwise reproduced without the author's permission.

AVIS:
L'auteur a accordé une licence non exclusive permettant à la Bibliothèque et Archives Canada de reproduire, publier, archiver, sauvegarder, conserver, transmettre au public par télécommunication ou par l'Internet, prêter, distribuer et vendre des thèses partout dans le monde, à des fins commerciales ou autres, sur support microforme, papier, électronique et/ou autres formats.

L'auteur conserve la propriété du droit d'auteur et des droits moraux qui protège cette thèse. Ni la thèse ni des extraits substantiels de celle-ci ne doivent être imprimés ou autrement reproduits sans son autorisation.

In compliance with the Canadian Privacy Act some supporting forms may have been removed from this thesis.

While these forms may be included in the document page count, their removal does not represent any loss of content from the thesis.

Conformément à la loi canadienne sur la protection de la vie privée, quelques formulaires secondaires ont été enlevés de cette thèse.

Bien que ces formulaires aient inclus dans la pagination, il n'y aura aucun contenu manquant.

Canada

Reproduced with permission of the copyright owner. Further reproduction prohibited without permission.

Gold-Induced Nanostructuring of Silicon Surfaces

By

Laura Pedri

ABSTRACT

In this thesis, a combination of scanning tunneling microscopy and low energy electron diffraction is used to investigate how submonolayer amounts of Au affect the large scale surface morphology of a vicinal Si sample miscut from (111) by 8° toward [11-2]. It is found that the structure of this surface is exquisitely sensitive to Au coverage. The surface exhibits nanofacets whose orientation depends critically on the amount of Au deposited. These nanofacets must preserve the total off-axis angle of the wafer. We find that the (775) facet persists over a wide range of Au coverages up to 0.32 ML. The (775)-Au reconstruction is characterized by a self-assembled array of 1-d atomic chains spaced 21.3 Å apart and is optimized at a Au coverage of 0.24 ± 0.03 ML. Oddly, the stoichiometry at optimal coverage incorporates 1.5 Au atoms per unit cell. The persistence of the (775)-Au reconstruction over such a wide range of Au coverages suggests that it is a low energy surface.

Reproduced with permission of the copyright owner. Further reproduction prohibited without permission.

TABLE OF CONTENTS

1. Introduction 3

2. Silicon Crystallography 6

3. Experimental Techniques 12

3.1. The Ultra High Vacuum System 12

3.2. Low Energy Electron Diffraction 15

Principles of Diffraction 16

Instrumentation 19

3.3. Auger Electron Spectroscopy 20

Principles of Auger Emission 20

Auger Spectra 22

Instrumentation 22

3.4. Scanning Tunneling Microscopy 24

Quantum Tunneling 24

Instrumentation 28

4. Sample Preparation 31

5. Results and Discussion 37

6. Summary 56

7. References 59

Reproduced with permission of the copyright owner. Further reproduction prohibited without permission.

1. INTRODUCTION

Interest in nanostructures is fueled by their unusual physical properties and by their potential use in ultra-small electronic devices[1]. An effective approach to fabricate such small structures is by self-assembly. One area of recent interest is the self-assembly of Au induced atomic wires on Si which may act as a prototype system to study the one dimensional confinement of electrons[2-9].

There have been many predictions concerning exotic electron behaviour in one dimension[5,10]. In particular, a quantum liquid in one dimension is known as a Luttinger liquid[11]. Here, elementary excitations are collective spin and charge density fluctuations with bosonic character, unlike Landau's Fermi Liquid Theory where they are quasi-particles with charge e and spin 1/2. For example, in two or three dimensions it is improbable that electron wave packets would ever penetrate each other. In one dimension, however, the Fermi surface is just two points with wavevectors $\pm\mathbf{k}_F$, and electrons are forced into collisions. Thus, the electron wavepackets have maximum overlap and excitation becomes a collective process.

Atomic scale wires not only produce exotic phenomena that are fundamentally interesting to study, they also offer tantalizing possibilities in modern technology. For these applications, atomic scale wires on Si are an ideal substrate since they are formed by a self-assembly process that results in a high degree of perfection. For example, Kirakosian et al.[3] have focused on incorporating DNA with these chains for the purpose of creating electronic biosensors for proteins, antibodies and viruses. Other possible applications include fabricating connections to muscle cells and neurons in logic circuits.

Reproduced with permission of the copyright owner. Further reproduction prohibited without permission.

Si is an attractive substrate for the formation of atomic scale wires for several reasons[12]. Firstly, according to the Peierls theorem a single string of atoms suspended freely in space will not exhibit 1-d metallic behaviour[13]. The atoms will instead form pairs creating a lattice deformation and open up a band gap. It is possible to avoid the Peierls transition by anchoring the atoms to a rigid substrate like Si. In this way, the elastic energy penalty for a pairing distortion may be prohibitively high. Secondly, the Si bandgap prevents metallic states at the surface from coupling to the bulk. In addition, Si exhibits a natural tendency toward the formation of anisotropic surface reconstructions. If the sample is slightly miscut from the (111) plane, the deposition of metal atoms can induce a single domain self-assembled array of chains[2,6]. For larger miscuts, the deposition of Au stabilizes high index facets resulting in a regular step array with one chain per terrace. As a result, the chains can achieve the ultimate limit of atomically thin 1-d metallic wires[14].

Previous work by Crain et al.[14] has focused on tuning the chain spacing by varying *both* the wafer miscut and the Au coverage. They selected four prototypical orientations: Si(335)-Au and Si(557)-Au which are oriented toward [-1-12], and Si(553)-Au and Si(775)-Au which are oriented toward [11-2]. In many respects, Si(775)-Au exhibited unique behaviour compared with the other chain structures. In particular, these authors reported that the Si(775)-Au reconstruction is stable over a wide range of Au coverages; 0.25 ± 0.07 ML. At the low end of this range, the stoichiometry is consistent with the incorporation of one Au atom per unit cell. On the other hand, the high end of this range, 0.32 ML, corresponds to over two Au atoms per unit cell. If the (775)-Au surface has a unique surface structure, and thus Au stoichiometry, it is not clear why it is

Reproduced with permission of the copyright owner. Further reproduction prohibited without permission.

observed over such a wide range of coverages. Other groups have also observed stable (775)-Au surfaces and have suggested that (775) is a low energy facet[15-17].

In this thesis, the Si(775)-Au reconstruction is investigated as a function of Au coverage in an attempt to gain insight into its peculiar behaviour. By using a constant miscut and only varying the Au coverage, we can observe how submonolayer amounts of Au affect the surface structure of the wafer. Using STM and LEED, we identify the resulting Au-induced facet planes, compose a phase diagram of the surface reconstructions and define the optimal coverage for the (775)-Au reconstruction.

Reproduced with permission of the copyright owner. Further reproduction prohibited without permission.

2. SILICON CRYSTALLOGRAPHY

Silicon is the most widely used semiconductor (indirect bandgap of 1.17eV) in electronics. In the bulk, the atoms form tetrahedral bonds and adopt a diamond crystal structure (fcc with a basis of 2) as shown in Figure 2.1. The primary cleavage plane is (111).

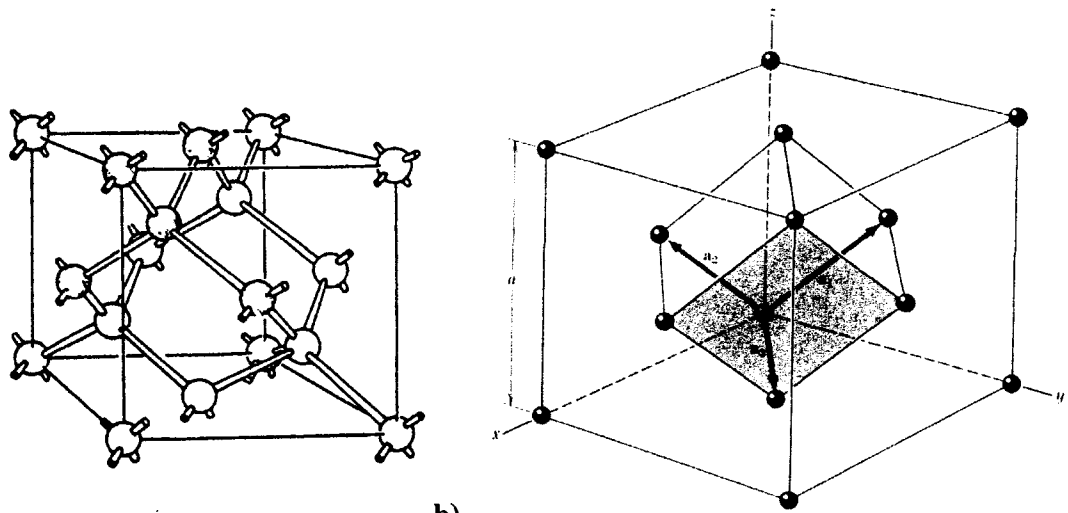

a) b)

Figure 2.1a) The silicon (diamond) structure[18] b) fcc structure showing primitive basis vectors[19]

The first semiconductor surface imaged with the scanning tunneling microscope (STM) was the Si(111)7x7 reconstruction[20]. The 7x7 reconstruction is the low energy surface for clean (111) below 850°C. Above this temperature, the surface reconstructs in a 1x1 pattern[21]. As discussed below, the large 7x7 unit cell is one of the reasons Si is an attractive template for the self-assembly of atomic chain structures.

The atomic structure of the Si(111)7x7 reconstruction has been the subject of debate since 1959 when the first LEED observations were published[22]. It wasn't until

Reproduced with permission of the copyright owner. Further reproduction prohibited without permission.

1985 that the widely accepted dimer-adatom-stacking fault (DAS) model was proposed by Takayanagi, et al. (see Figure 2.2)[23].

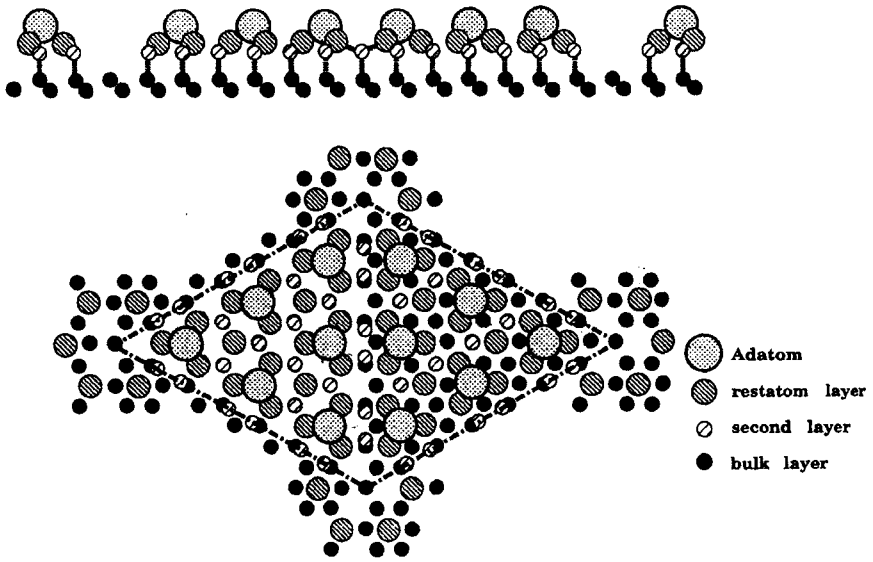

Figure 2.2. Schematic of the Si(111)-7x7 DAS structure showing the faulted and unfaulted halves[24].

The DAS model involves considerable rearrangement of both the surface atoms and top double-layer atoms. In total, there are 49 atoms in the surface reconstruction split into two halves, one being 0.2 Å higher than the other. These are referred to as the faulted and unfaulted halves respectively. Dimers occur at the interface between the halves and work to 'zip' the faulted and unfaulted halves together. There are 18 dimers in all. The protrusions visible in STM are the 12 top-layer adatoms that are each bonded to three atoms in the surface double-layer. Note that this surface is three-fold symmetric.

The adsorption of Au on the 7x7 reconstruction induces a host of reconstructions depending on the Au coverage. At a Au coverage of 0.44 ML, the surface undergoes a 5x2 chain-like reconstruction characterized by chains spaced 16.7 Å apart[25].

Reproduced with permission of the copyright owner. Further reproduction prohibited without permission.

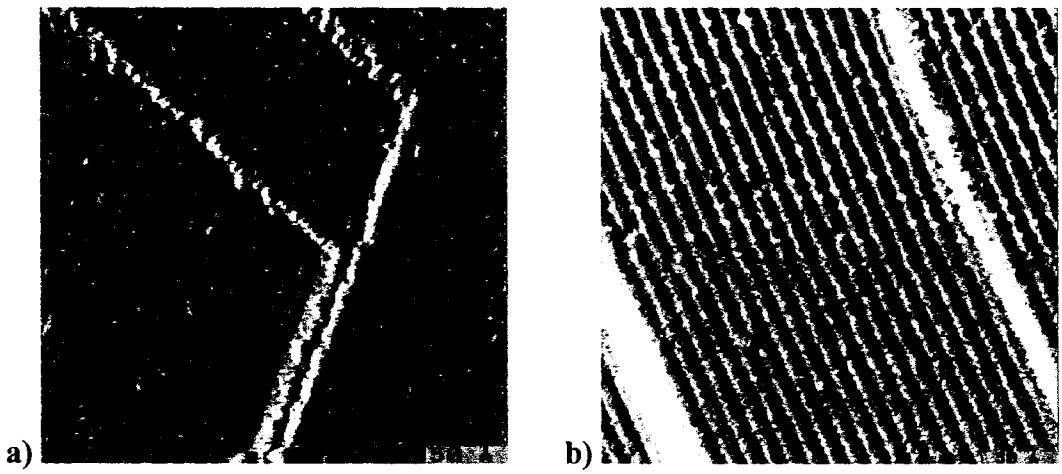

Figure 2.3a) Multidomain Si(111)5x2-Au, 298 Å x 291 Å b) A single domain Si(111)5x2-Au on a 1° off-axis Si(111) sample, 307 Å x 306 Å. Both images are presented as the derivative of topography which gives the appearance of a surface illuminated from the left. In this case, light appears to shine on the steps.

Due to the underlying three-fold symmetry of the surface, the 5x2 exhibits three equivalent domains of chains along the, [1-10], [01-1] and [-101] directions. The domain structure limits the overall length of the chains (see Figure 2.3a). A sample with a slight miscut away from the (111) plane will form an array of steps and break the symmetry of the surface. Since the 7x7 reconstruction is large and has a stable step geometry[2,5,6] the top edge of a step will always consist of a string of corner holes of the 7x7 unit cell which run along [-110]. Since the 7x7 reconstruction on any terrace is single domain, a kink in the step edge equals the addition of a 1/2-unit cell to reach another row of corner holes. This is equivalent to the addition of 14 rows of Si atoms and generates a large energy barrier to kink formation ensuring long, straight step edges. If the steps are chosen to run parallel to one of the chain directions, (in our case, [1-10]), the chains align parallel to the steps. The result is a self-assembled array of Au-induced chains that essentially run the breadth of the entire sample (see Figure 2.3b). At high miscut angles, the unit cell contains a step edge and one can achieve the ultimate limit of one chain per terrace[26].

Reproduced with permission of the copyright owner. Further reproduction prohibited without permission.

Following the lead of previous authors we employ the following nomenclature for vicinal surfaces[27]. We will refer to the clean vicinal surface by the Miller indices appropriate for the surface normal to that plane. For the Au-induced surface, we will use the same Miller index to describe the surface adding the suffix '-Au' to the name. Unfortunately, this standard can be confusing since the names of both reconstructions are extremely similar, although the surfaces are structurally very different. For example, the clean (775) facet corresponds to a miscut 8.5° from (111) toward [11-2]. This facet is unstable. The incorporation of Au on this surface induces a wholesale reconstruction that stabilizes the facet and results in highly reconstructed (111) terraces spaced 21.3 Å apart separated by single bilayer steps. We label this the (775)-Au surface.

A vicinal surface will only be stable if the total free energy cannot be lowered by the creation of facets. The net angle of the surface must be conserved and the net area of the facets can be determined using the following equation[28].

$$A\vec{n} = \sum_i A_i \vec{n_i} \tag{2.1}$$

where $\vec{n}$ is the surface normal, A is the area of the original surface and A_i are the areas of the resulting facets. In addition, if the faceting process is reversible the morphological changes can be conveniently described by equilibrium thermodynamics[28]. The resulting surface morphology is a consequence of the thermodynamic balance between surface elastic energy and the reduction of dangling bonds. In vacuum, faceting is achieved via surface self diffusion where the rate limiting mechanism is the evaporation/condensation of mobile species on the terraces[29]. Schwennicke et al.[30] has found that metal adsorbates on Si induce profound modifications of step-step interactions and thus, the morphology of the surface. Previous work[15-17] has found that annealing submonolayer amounts of Au

Reproduced with permission of the copyright owner. Further reproduction prohibited without permission.

on vicinal Si(111) preferentially causes faceting to (775) and (995) planes suggesting that these are low energy configurations.

In this thesis, we study the surface structure of an 8° off-axis wafer as a function of Au coverage. We find that the Si(775)-Au reconstruction dominates the surface morphology. Figure 2.4 illustrates a previously proposed structure[14] for the (775)-Au reconstruction and an associated STM image obtained in our laboratory. In the STM image, the chains are seen as bright lines running vertically across the image in the [1-10] direction. Photoemission experiments by Crain et al.[14] have revealed that these chains exhibit 1-d metallic behaviour. The bright spherical protrusions are Si adatoms. In the structural model, the Au atoms are represented by yellow spheres and the Si atoms by red and blue spheres. Although the structure of the (775)-Au reconstruction has not been definitively determined, it is generally agreed that the unit cell (and effectively, each chain) is a highly reconstructed Si(111) terrace separated by a single bilayer step (3.1 Å)[14]. It is known that it is energetically favourable for Au atoms to become

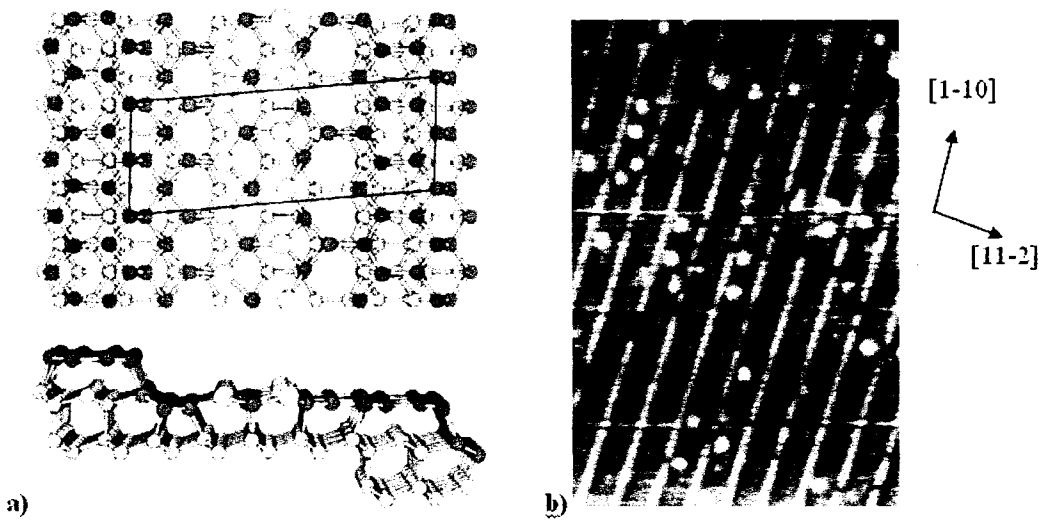

Figure 2.4a) Proposed structure for the Si(775)-Au reconstruction taken from Crain et al. showing the unit cell and, b) an STM image of the Si(775)-Au reconstruction, 158 Å x 237 Å, -2.0V.

Reproduced with permission of the copyright owner. Further reproduction prohibited without permission.

incorporated into the terrace and substitute for Si atoms in the surface layer rather than sit on top of the terrace near the step edge[31,32]. Calculations show that the Au states are well below E_F , thus, the Au is inaccessible to the STM tip. Therefore, all structures in the STM images are associated with Si states. This includes the adatoms, which, on a related surface, were also experimentally determined to be Si[12,33]. The unit cell incorporates a step edge and also includes the honeycomb-chain-channel (HCC) reconstruction which is the Si analogue of graphite[34]. The red spheres in the above model represent the HCC reconstruction. In addition, Crain et al. suggest that two Au atoms are assigned to each terrace. This assignment was based on similarities between photoemission data for the Si(775)-Au and the Si(111)5x2-Au surfaces[14]. The (5x2)-Au reconstruction is known to have two Au atoms per unit cell[32]. Although the (775)-Au reconstruction exhibits many similarities with the (5x2)-Au unit cell, the exact stoichiometry of the (775)-Au unit cell is unknown.

Reproduced with permission of the copyright owner. Further reproduction prohibited without permission.

3. EXPERIMENTAL TECHNIQUES

3.1. The Ultra High Vacuum System

The study of surface science, as a whole, requires an environment in which atomically clean surfaces can be prepared and maintained. As a result, the science has largely benefited from the development of ultrahigh vacuum (UHV) technology. A clean sample will not acquire much contamination for the duration of an experiment in a UHV system. The time for one complete monolayer to adsorb onto a surface, assuming each incident molecule sticks, depends inversely on pressure and is given by

$$T_{ML} = 4kT/Pvd_o^2 \qquad (3.1)$$

where T is the temperature, ν is the average velocity of the molecules, P is the pressure, k is Boltzmann's constant and d_o^2 is the surface area occupied by each molecule. For air, d_o is 0.372 nm and ν is 467 m/s at room temperature, therefore, at atmosphere it would take just 25 ns to cover a sample, as opposed to over 5 hours under UHV conditions[35]. Clearly, cleanliness is the most important attribute that distinguishes a UHV system from any other vacuum system.

A UHV system uses a combination of pumps to evacuate the chamber. Each pump has its own specific operating pressure range and its own characteristic class of gases that it will pump and also generate as impurities. A schematic of the vacuum system used in this experiment is shown in Figure 3.1. The first stage of pumping occurs in the mechanical pump. Gas enters the pumping chamber and is compressed by a rotor and vane and then expelled to the atmosphere through a discharge valve. It has a high pumping speed but a low pressure limit in the high vacuum range. The pump used in the laboratory was an Edwards E2M2[36].

Reproduced with permission of the copyright owner. Further reproduction prohibited without permission.

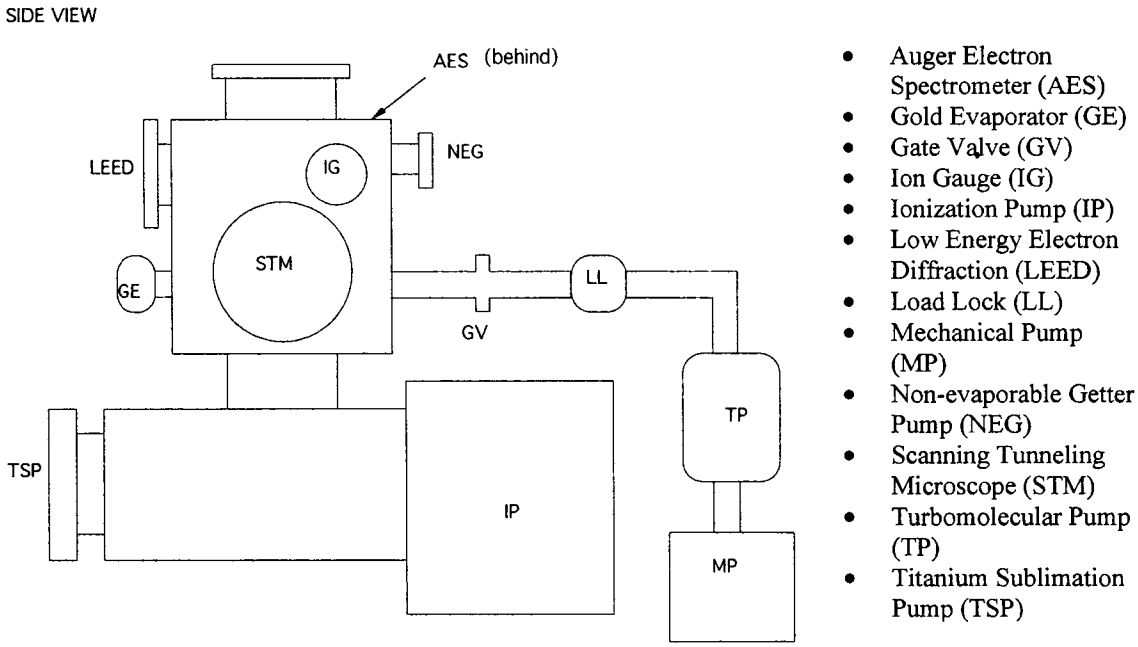

Figure 3.1. A simplified schematic of our UHV system. View ports and manipulators were omitted for simplification.

The next stage of pumping is done by the turbomolecular pump, which works on the principle of momentum transfer. The turbo's rotating blades impart momentum to gas molecules in a preferential direction such that the probability of a molecule being transmitted from the inlet to the outlet is much higher than in the reverse direction. A single blade is insufficient to produce suitably low pressures, so multiple blades and multiple stages are used to achieve high vacuum. In general, turbo pumps have a high pumping speed, large hydrogen compression ratio, low ultimate pressure and do not backstream hydrocarbons. Due to the nature of its operation, a turbo pump is most efficient in the molecular flow regime where $Kn > 1$. Knudsen's number, Kn, is the ratio of the mean free path of a gas molecule to some characteristic dimension of the system. As a result, it cannot exhaust air to the atmosphere and must be backed by a mechanical pump. The pump used in the laboratory was a Varian Turbo-V60 Turbomolecular

Reproduced with permission of the copyright owner. Further reproduction prohibited without permission.

Pump[37]. The base pressure is 8 x 10^{-10} Torr. The turbomolecular pump was mainly used to back the ion pump during chamber baking and for pumping out the load lock.

To achieve even lower pressures, the turbo molecular pump is separated from the chamber via a gate valve, and then the ion pump is used. Ions can be generated at low pressures if the energizing electrons can be made to hit a gas molecule before they hit a wall. Ion pumps achieve this by using a Penning Cell, which consists of an anode and two cathodes. Electric fields present in each cell trap the electron in a potential well between the two cathodes and an axial magnetic field forces the electrons into circular orbits that prevent them from reaching the anode. Thus, electrons travel long distances before colliding with the anode increasing the probability of colliding with and ionizing a gas molecule. Ions produced in a collision are accelerated to the cathode where they stick, sputter away the cathode (in our case a titanium cathode) and produce secondary electrons leaving the cathode to getter active gases. The ion pump used in the laboratory was a Varian VacIon Plus 150 with a base pressure of 10^{-11} Torr[37].

Working in tandem with the ion pump are the titanium sublimation pump (TSP) and the non-evaporable getter pump (NEG). The TSP is classified as a surface getter pump. An ac current is used to heat a titanium filament that sublimes and deposits titanium on adjacent walls. Since titanium is reactive, active gases are captured on the freshly sputtered titanium surface. A fresh titanium layer must be periodically deposited to maintain constant pumping. The TSP used in the laboratory was manufactured by Varian[37].

The NEG works on principles similar to the TSP but without the sublimation process. The pump itself is made of a gettering material that can be activated or

Reproduced with permission of the copyright owner. Further reproduction prohibited without permission.

regenerated by heat. A Capacitorr-D400 NEG pump[38] was used in the laboratory. The cartridge is made of a series of disks made of a sintered porous material. A tungsten wire is used to heat the cartridge and activate the material for pumping by diffusing adsorbed carbides and oxides into the bulk.

Despite the efficiency of the network of pumps used in the system, the base pressure would still not reach the low pressures that characterize a UHV system. This is because water vapor adsorbs onto and absorbs into the walls of the chamber. These molecules slowly desorb when the system is being pumped down and limit the base pressure. To eliminate water vapor, it is therefore necessary to bake the chamber to at least 100°C for a minimum of 48 hours[39]. Following the bake, pressures of 10^{-11} Torr can be obtained.

To measure the low pressures characteristic of a UHV chamber we use an ionization gauge. Although it is not a pump, the ion gauge works on principles similar to that of the ion pump and is used to measure pressures below 10^{-3} Pa. Electrons, when passing through the interior of a grid, ionize gas molecules. These ionized molecules are then accelerated by the grid system to a thin wire collector located in the centre of the grid at a rate proportional to the gas density. The gauge used in the laboratory is a Varian UHV-24 Nude Ionization Gauge[37]. It gives accurate measurements from 10^{-3} Torr to $2x10^{-11}$ Torr at its x-ray limit.

3.2. Low Energy Electron Diffraction

One method we used to study crystal surface structure was low energy electron diffraction (LEED). LEED is the oldest of all surface science techniques. Davisson and

Reproduced with permission of the copyright owner. Further reproduction prohibited without permission.

Germer won the Nobel Prize in 1937 for demonstrating the wave nature of the electron using a LEED experiment[40]. Interest in LEED grew in the 1960's due to the development of modern UHV technology and direct visual display of the diffraction pattern. The physical basis of LEED lies in the interference effects produced by phase differences between electrons elastically scattered from the 2-dimensional array of atoms on the crystal surface. Low energy electrons have a wavelength on the order of the lattice spacing of the surface. Thus, when an electron beam is aimed at the sample the electrons are scattered by the strong potential produced by the positive nucleus and outer electrons of the atom.

Low energy electrons have a short mean free path, which means electrons penetrating more than a few atomic layers into the solid have a high probability of being inelastically scattered. The probability of backscattering is also high, so few electrons will actually penetrate the surface. The elastically scattered electrons can be seen as a Fraunhofer diffraction pattern on a phosphor screen.

Principles of Diffraction

To examine the diffraction process more closely, imagine that the surface atoms on a crystal are arranged in a perfect 2-dimensional periodic lattice that will act as a grating. One method used to determine the momentum of the diffracted rays, Ewald's construction, exploits conservation of momentum. A 3-dimensional unit cell of a crystal can be defined by three lattice vectors $\mathbf{a}_1$, $\mathbf{a}_2$, and $\mathbf{a}_3$ (see Figure 2.1b). The reciprocal lattice vectors are given by

Reproduced with permission of the copyright owner. Further reproduction prohibited without permission.

$$\mathbf{b}_1=2\pi(\mathbf{a}_2\mathbf{x}\mathbf{a}_3)/V \quad (3.2)$$

$$\mathbf{b}_2=2\pi(\mathbf{a}_3\mathbf{x}\mathbf{a}_1)/V \quad (3.3)$$

$$\mathbf{b}_3=2\pi(\mathbf{a}_1\mathbf{x}\mathbf{a}_2)/V \quad (3.4)$$

where $V=\mathbf{a}_1\cdot\mathbf{a}_2\mathbf{x}\mathbf{a}_3$. To obtain a 2-d reciprocal lattice of the surface, let the base vector $\mathbf{a}_3$ of the 3-d crystal structure approach infinity and $\mathbf{a}_1$ and $\mathbf{a}_2$ remain unchanged. As a result, the reciprocal lattice vector $\mathbf{b}_3$ approaches 0, and the discrete points parallel to $\mathbf{b}_3$ in the reciprocal lattice coalesce to form lines or rods as shown in Figure 3.2.

For the 2-d diffraction of backscattered electrons from solids

$$\mathbf{k}' = \mathbf{k} + \Delta\mathbf{k} \quad (3.5)$$

Using the origin of k as the centre, a sphere of radius $2\pi/\lambda$ is constructed in reciprocal space.

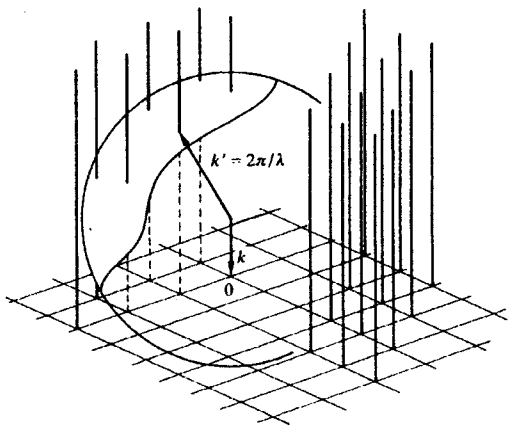

Figure 3.2. Ewald sphere within the 2-d reciprocal lattice[41]

Diffraction occurs everywhere the Ewald sphere cuts a reciprocal lattice rod, since this is where Equation 3.5 is satisfied. By varying the incident beam energy the number of scattered beams and their directions will change. The lateral symmetry of the surface

Reproduced with permission of the copyright owner. Further reproduction prohibited without permission.

is immediately reflected in the geometry of the diffraction pattern. LEED, therefore, can provide information on the periodicity and translational symmetry of a surface.

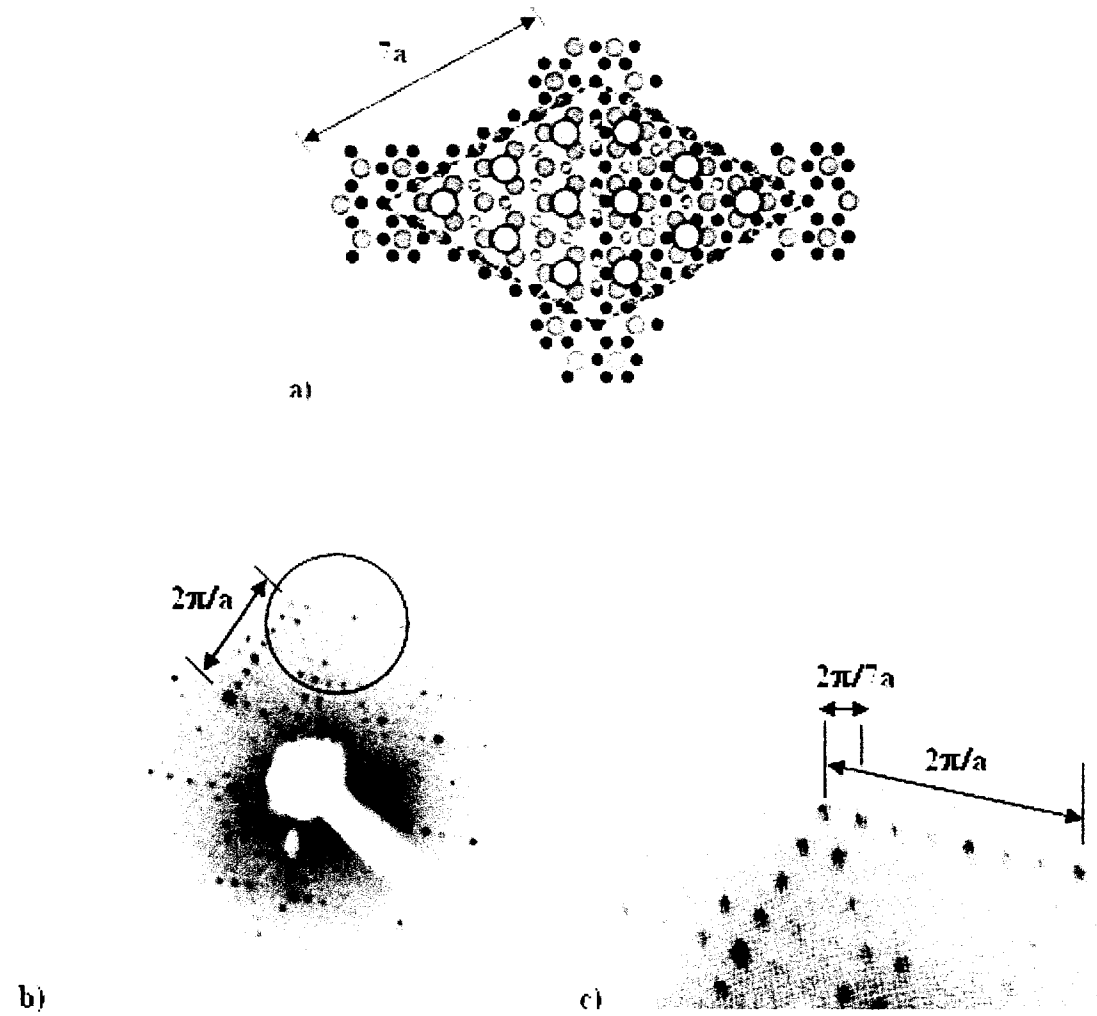

Figure 3.3a) Real space 7x7 reconstruction[24]. b) LEED pattern showing the 7x7 reconstruction in reciprocal space. c) Area defined by the circle in (b) showing the reciprocal lattice vector.

For example, the clean Si(111) surface exhibits a 7x7 reconstruction, which means that the surface layer is described by a unit cell seven times larger than the bulk

Reproduced with permission of the copyright owner. Further reproduction prohibited without permission.

termination. Thus, the real space unit cell is defined by vectors $|\mathbf{a}|=7a$, and the reciprocal lattice vector is then $|\mathbf{b}_i|=2\pi/7a$ as illustrated in Figure 3.3.

Instrumentation

A simplified schematic of the LEED set-up used in this experiment[42] is shown below.

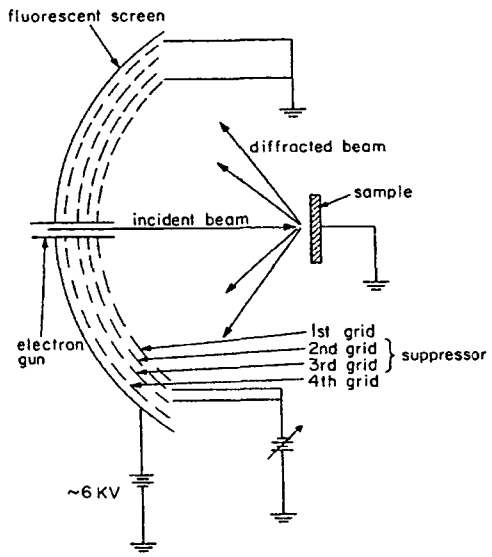

Figure 3.4. Simplified LEED schematic[43]. See text for details.

An electron gun provides the incident electron beam that is then focused to a grounded target surface. Diffracted electrons travel in a field free region toward a system of grids, the first of which is set to the same potential as the sample (ground). The next few grids are biased to retard all electrons except those that have been elastically scattered. The diffracted electrons pass through these grids and are accelerated onto a fluorescent screen. The observed diffraction pattern is a projection of the reciprocal lattice of the surface. The diffraction pattern is recorded using a digital camera purchased

Reproduced with permission of the copyright owner. Further reproduction prohibited without permission.

from Electrim Corporation[44] and externally controlled using a previously developed LABVIEW[45] program[46].

3.3. Auger Electron Spectroscopy

Principles of Auger Emission

Another method used to study the crystal surface is Auger electron spectroscopy. Auger electron emission can be triggered by the ionization of a core level of an atom by an incident electron or photon. An ion in such an excited state can lose some of its potential energy by filling the core hole with an electron from a higher energy level and by emitting energy in the form of either a photon or an electron (see Figure 3.5). These two emission processes compete. Photon emission dominates when the electron binding energy is greater than 10keV[47]. Electron emission is the more probable decay mechanism for low atomic number elements with an n = 1 vacancy and for all elements with n = 2 and n = 3 vacancies.

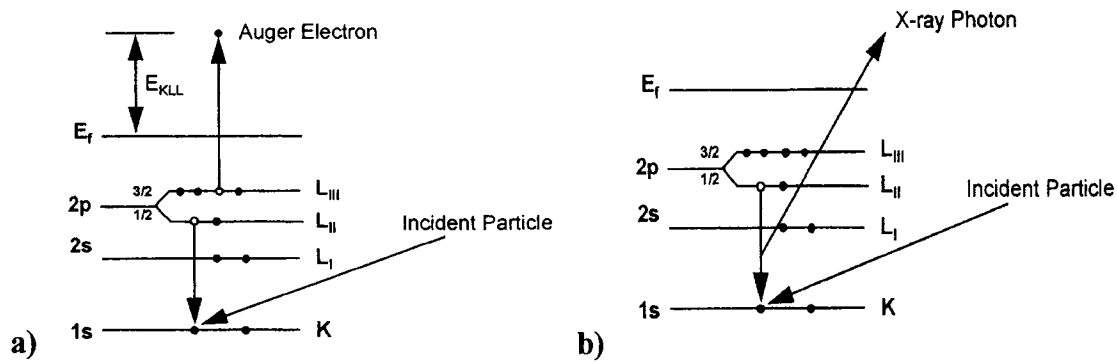

Figure 3.5a) For Auger emission, the core hole is filled with an electron from a higher energy level and the energy difference between the states (in this case, the K and L_{II} levels) is carried away by the Auger electron. b) For photon emission, the difference between the K and L_{II} states is carried away by a photon[48].

Reproduced with permission of the copyright owner. Further reproduction prohibited without permission.

In the electron emission process, the vacancy is filled by an electron in a higher energy level. The energy difference between the states is carried away by a third electron since this electron must expend energy to escape the atom. The emitted electron is known as the Auger electron, named after Pierre Auger who described this process in 1925[49]. For Auger emission, the emitted electron will have a kinetic energy, KE, which depends on the energy of the atomic levels involved in the process as

$$KE = E_a - E_b - E_c - U \tag{3.6}$$

E_a, E_b and E_c are the one electron binding energies of the core electron, the valence electron and the Auger electron respectively. U lumps together the hole-hole interaction energy in the free atom, and any screening polarization and relaxation effects in the solid[47]. From Equation 3.6, the Auger electron has a discrete energy characteristic of the energy levels of a specific atomic species making spectroscopic identification of the element possible.

AES is highly surface specific. Auger emission fills holes of low binding energy giving the Auger electrons a short mean free path. Thus, electrons emitted from deeper within the solid have a low probability of detection. AES can detect surface contaminants down to the 10^{12} atoms/cm^2 range[50], however it cannot detect the presence of hydrogen or helium due to the fact that Auger emission is a three electron process. AES is an extremely sensitive tool to determine atomic species present at a surface. We use AES in tandem with LEED as powerful tools to provide detailed information on the organization and purity of our surfaces at the atomic scale.

Reproduced with permission of the copyright owner. Further reproduction prohibited without permission.

Auger Spectra

An Auger electron spectrum plots the number of electrons detected as a function of energy, N(E) vs. E. Elements are identified by the location of a small peak on the energy axis. The width of the Auger peak is affected by the type of transition (how many valence levels are involved), the lifetime of the transition and small energy losses experienced by the escaping electron. The numerous energy losses create a tailing structure on the low energy side of most peaks on the N(E) curve and, combined with the fact that the peak is small, makes the peak maximum difficult to locate. To solve this problem dN(E)/dE is often plotted instead. Peak energies are detected by the location of the most negative part of the Auger spike on the dN(E)/dE axis.

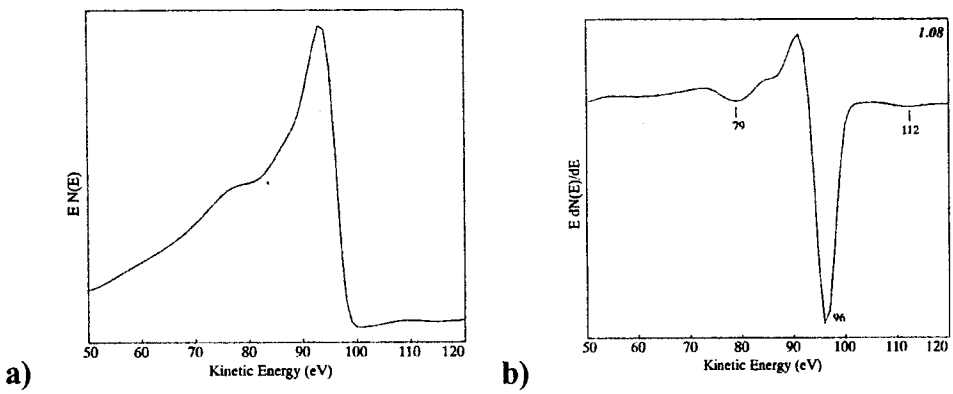

Figure 3.6a) Auger spectrum plotted as intensity vs. energy b) Auger spectrum plotted as the derivative of the intensity vs. energy. Note how, in this case the peak is sharp making spectroscopic identification more straightforward[48].

Instrumentation

The Auger electron spectrometer used in this experiment is an Omicron model CMA 100[51] and is located inside the UHV chamber. The CMA (cylinder mirror analyzer) consists of concentric metal cylinders that are biased to produce an electric

Reproduced with permission of the copyright owner. Further reproduction prohibited without permission.

field designed to guide electrons of a particular energy to a detector. An energy spectrum is swept by varying the potential of the outer cylinder, which thereby samples the energy distribution of the electrons that hit the detector. In these experiments, a 3000 eV electron beam was used as the incident beam and the emitted electrons were collected by the CMA and output to a channel electron multiplier (Channeltron). The Channeltron is a thin tube of a low electron binding energy material. A high voltage is applied between the ends of the tube establishing a continuous voltage gradient. Incident electrons trigger the emission of secondary electrons which proceed further into the Channeltron triggering more electrons, and so on.

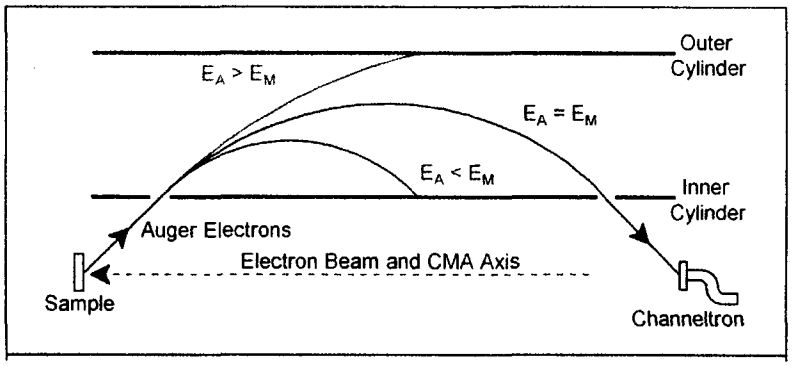

Figure 3.7. Simplified schematic of a CMA[48]. The potential of the outer cylinder can be varied to sample the Auger electron energy distribution.

This process can increase the detected electron current by a factor of 10^7 [52]. The resulting spectrum is graphically displayed using the DAT software package supplied with the instrument. The Handbook of Auger Electron Spectroscopy 3rd Ed.[48] was used as a standard to compare with the experimentally determined spectra and to identify elements present on the surface of the Si wafer.

Reproduced with permission of the copyright owner. Further reproduction prohibited without permission.

3.4. Scanning Tunneling Microscopy

Scanning tunneling microscopy (STM) was first performed in 1981 by Binning, Rohrer, Gerber and Weibel at IBM Zurich Laboratories. In 1982, they published STM images of the Si(111) 7x7 reconstruction thereby ending a 20 year debate concerning the structure of this surface[53]. In 1986 they won the Nobel Prize for this work.

In STM, a metal probe with an atomically fine tip is brought close to the conducting surface to be imaged. When a voltage less than the work function of the material is applied, electrons can tunnel across the gap. The net current is in the direction of the bias. Although this process is classically forbidden it occurs according to the principle of quantum tunneling.

Quantum Tunneling

In an STM system operating under vacuum, the space in the vacuum region acts as a potential barrier between the metallic tip and surface.

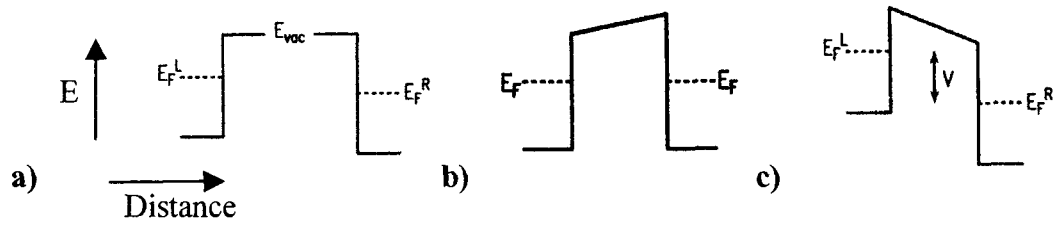

Figure 3.8. A schematic of the potential barrier between electrodes L and R for vacuum tunneling[54]. a) The difference in the Fermi levels is equal to the difference in the work functions between L and R. b) The system approaches electrical equilibrium. c) A voltage is applied across the gap and tunneling can occur in the direction of the bias.

The difference between the Fermi levels is equal to the difference in work functions between the two metals (see Figure 3.8a.). The system will approach electrical equilibrium, and the difference in work functions is manifested as an electric field across

Reproduced with permission of the copyright owner. Further reproduction prohibited without permission.

the gap (see Figure 3.8b.). When a voltage, V, is applied across the gap, electrons in states within an energy eV below the Fermi level on the negative side can tunnel into empty states up to an energy eV above the Fermi level on the positive side (see Figure 3.8c). The fraction of electrons that tunnel across the gap (the transmission probability) can be determined by solving Schrödinger's equation for a 1-d potential barrier.

Consider a beam of identical particles incident on a potential barrier of height U and width L as in Figure 3.9.

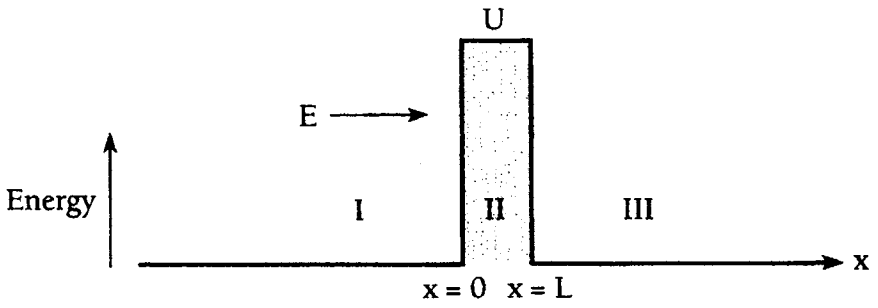

Figure 3.9. 1-d potential barrier[54]

It is well known that the tunneling current at low voltage and temperature behaves as

$$I \sim e^{-2\kappa d} \tag{3.7}$$

where $\kappa=(2m(U-E)/\hbar^2)^{1/2}$. For a typical work function of around 4 eV, the inverse decay length, κ, is on the order of 1.0 $Å^{-1}$. Thus, the tunneling current will drop nearly an order of magnitude for every Ångstrom of vacuum between the surface and the tip. Since the current is sensitive to changes in height at the Ångstrom level, using feedback control to maintain a constant tunnel current between the tip and sample while raster scanning the tip across the sample will give a topographical map of the surface. This is true so long as

Reproduced with permission of the copyright owner. Further reproduction prohibited without permission.

the surface features are on the nanometer scale or larger, such as terraces and atomic steps. On an atomic scale, the definition of topography becomes obscure and a more precise calculation of the tunneling current is needed.

Tersoff and Hamann developed a theory for tunneling between a surface and a model tip in their 1985 paper entitled *Theory of the scanning tunneling microscope*[55]. While they treat the surface 'exactly', the tip is modeled locally as a spherical potential well due to the fact that tip manufacturing was (and still is) performed in a non-reproducible manner. According to Bardeen[56], the tunneling current is given by

$$I = \frac{2\pi e}{\hbar} \sum_{\mu,\nu} f(E_\mu)\left[1 - f(E_\nu + eV)\right] \left| M_{\mu\nu} \right|^2 \delta(E_\mu - E_\nu) \tag{3.8}$$

where f(E) is the Fermi function, V the applied voltage, M_{uv} the tunneling matrix element between states ψ_u (probe) and ψ_v (surface) and E_u and E_v is the energy of state ψ_u and ψ_v respectively in the absence of tunneling. Note that, ψ_u and ψ_v are not orthogonal and are of different Hamiltonians. In the limit of small voltage, room temperature, and replacing the tip with an ideal point source of current, Equation 3.8 reduces to[55]

$$I \propto \sum_{v} \left| \psi_v(\bar{r}_0) \right|^2 \delta(E_v - E_F) \tag{3.9}$$

where $\bar{r}_0$ is the position of the probe. The quantity on the right of Equation 3.9 is the surface local density of states (LDOS) at the Fermi energy. Thus, the STM image is a contour map of constant surface LDOS.

The problem of a non-ideal tip can be solved if M_{uv} is calculated for this general case. Tersoff and Hamann[55] obtained, under the assumption that any angular dependence of ψ_u can be neglected, an expression for M_{uv} and evaluated it to be

Reproduced with permission of the copyright owner. Further reproduction prohibited without permission.

$$M_{\mu\nu} = \frac{\hbar^2}{2m} 4\pi\kappa^{-1}\Omega_t^{-1/2}\kappa \mathrm{Re}^{\kappa R}\psi_\nu\left(\vec{r}_0\right) \tag{3.10}$$

where κ is the inverse decay length for the wavefunctions in vacuum, Ω_t is the probe volume and R is the local radius of curvature of the probe at $\vec{r}_0$. Now, the tunneling current becomes

$$I = 32\pi^3\hbar^{-1}e^2V\varphi^2 D_t\left(E_F\right)R^2\kappa^{-4}e^{2\kappa R} \times \sum_\nu \left|\psi_\nu\left(\vec{r}_0\right)\right|^2 \delta\left(E_\nu - E_F\right) \tag{3.11}$$

where D_t is the density of states per unit volume of probe tip, φ is the work function and E_F is the Fermi level. Thus, the tunneling current is proportional to the local density of states (LDOS), and the image is not directly associated with surface topography. Although Equation 3.11 ignores angular momentum, Tersoff and Hamman[55] and later Lang[57] showed that only s states (where m = 0) contribute appreciably to the tunnel current. Lang also supported Tersoff and Hamman's assertion that at low bias, the STM image is that of the surface LDOS at the position of the tip. Another interesting finding, according to Lang[57,58], is that the majority of the tunnel current is emitted from the furthermost atom jutting from the tip and is largely insensitive to the structure of the rest of the tip.

The fact that the STM images electronic states and not simply topography can be seen in the Au-induced chain-like reconstructions studied in this thesis. As was previously discussed, the Au states are inaccessible to the STM tip since Au derived states lie well below E_F. Therefore, all structures in the STM image are Si related (see Figure 2.4). The creators of the model shown in Figure 2.4 suggest that the bright chains are most likely related to Si dangling bonds at the step edge[14,32]. Thus, the chains are not

Reproduced with permission of the copyright owner. Further reproduction prohibited without permission.

actually topographical features but are directly related to the electronic structure of the surface.

Instrumentation

Figure 3.10 is a simplified schematic of an STM system. In STM, the current and

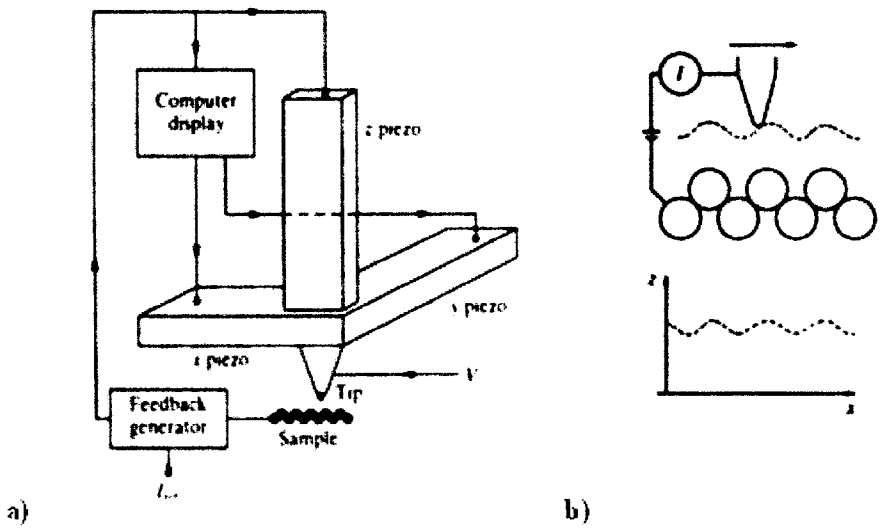

Figure 3.10 a) Simplified schematic of an STM system[47]. b) Constant current scanning mode[47]. The current and voltage between the tip and the sample is held constant as the tip is raster scanned across the sample.

the voltage between the sample and the tip are held constant as the tip is made to traverse the sample. Feedback control changes the distance between the sample and tip to maintain a constant current. This method is referred to as *constant current mode* (see Figure 3.10b) and was historically the first method to be used. Another method, the constant height mode, measures changes in current while the tip traverses the sample at a constant height. Although this method is faster, it runs the risk of crashing the tip into sample surface features and was not used in this thesis.

Reproduced with permission of the copyright owner. Further reproduction prohibited without permission.

The tip must be brought into tunneling range in a very precise manner and raster scanned without crashing into the sample. In addition, the spacing between tip and sample must be accurate to within 0.05 Å. These stringent tolerances are obtained using piezoelectric ceramics (see Figure 3.10a) that can be controlled by changing the voltage applied to the piezo. Independent movement in x, y and z, as well as mechanical rigidity to increase vibration isolation and feedback control make these ceramics particularly suited to the STM application. Piezoceramics actually have a non-linear response to applied voltage, but since the electric fields used in STM are small, the movement can be considered linearly proportional to the applied voltage.

A course approach mechanism must be used to bring the tip into tunneling range from a macroscopic distance away without crashing the tip. Our STM uses an inertial approach system. A voltage is applied to a piezo stack causing it to extend in the desired direction of motion. The scan tube maintains static friction and moves with the piezo stack. The stack then quickly slips back fast enough to overcome static friction. The scan tube's inertia maintains its position while the stack is in motion. The result is a net displacement of the scan tube but not the piezo stack. To prevent the tip from crashing into the sample on approach, the feedback contracts the scan tube and moves the tip away from the sample during the inertial step. It relaxes back after the step and, if no tunnel current is detected the process repeats.

Perhaps the most crucial part of the STM system is the tip itself. The best images are obtained when tunneling occurs from an atomically sharp tip. This condition is difficult to ascertain, but fortunately certain metal wires, when cut or fractured, produce a ragged surface with a high probability of having a single atom at the endpoint. The

Reproduced with permission of the copyright owner. Further reproduction prohibited without permission.

geometry, chemical nature of the tip and the behaviour of LDOS influence the resolution of the instrument. The resolution is limited by the size of the tip if the tip radius is greater than the tip-sample separation. However, in the case of an atomically sharp tip, the resolution is limited by the tip-sample separation. As tips, we used electrochemically etched tungsten or cut platinum-iridium wires. Both of these were used for data acquisition in this thesis.

Factors other than tip radius and placement also must be considered. Vibration isolation is absolutely necessary if atomic resolution is to be achieved and can be quite difficult to control. In the UHV system, the 'no moving parts' rule is employed when the STM is in use. This restricts the use of the turbomolecular pump and reactivation of the TSP. The STM sits on a Viton stack inside of the chamber to dampen any vibrations. In addition, the entire UHV system is pneumatically levitated.

The advantage of using STM, as opposed to using LEED and AES, is that it offers direct real-space determination of surface structure regardless of periodicity. Since it can be performed under UHV conditions it is particularly conducive to imaging our Si samples which are highly reactive in air. The STM used in this thesis was an Omicron Micro SPM[51] controlled by RHK Technology[59] SPM 100 electronics.

Reproduced with permission of the copyright owner. Further reproduction prohibited without permission.

4. SAMPLE PREPARATION

Several parameters affect the formation of regular step arrays on vicinal Si surfaces: miscut angle, annealing sequence, current direction and external stress[2]. All of these factors were strictly controlled using the following sample preparation procedure. The goal is to prepare clean samples that display a long range ordered array of atomically straight single height steps.

The substrate is n-type Si(111) with a miscut of 8° along (11-2)[60]. The doping concentration was in the 10^{18} cm^{-3} range. We also used n-type Si(111) miscut by 1° toward (-1-12) for calibration purposes. The wafers were held as stress free as possible between two Ta wire loops in a sample holder that was specially designed for this purpose (see Figure 4.1). The sample holder was designed so that each side was electrically isolated from the other to permit current flow through the sample when held between the two wire loops. The size of the holder is such that it fits into pre-existing sample transfer mechanisms inside the UHV chamber. Similar to the sample holder, one of these sample transfer mechanisms (*a.k.a. the thermal dis-combobulator*) was modified so that each side is electrically isolated to ensure that current is passed through the sample (see Figure 4.2). The sample was heated by a DC current and mounted such that current flows in the [1-10] direction. This direction avoids electromigration effects which cause kinks in the step edges to form[6].

Reproduced with permission of the copyright owner. Further reproduction prohibited without permission.

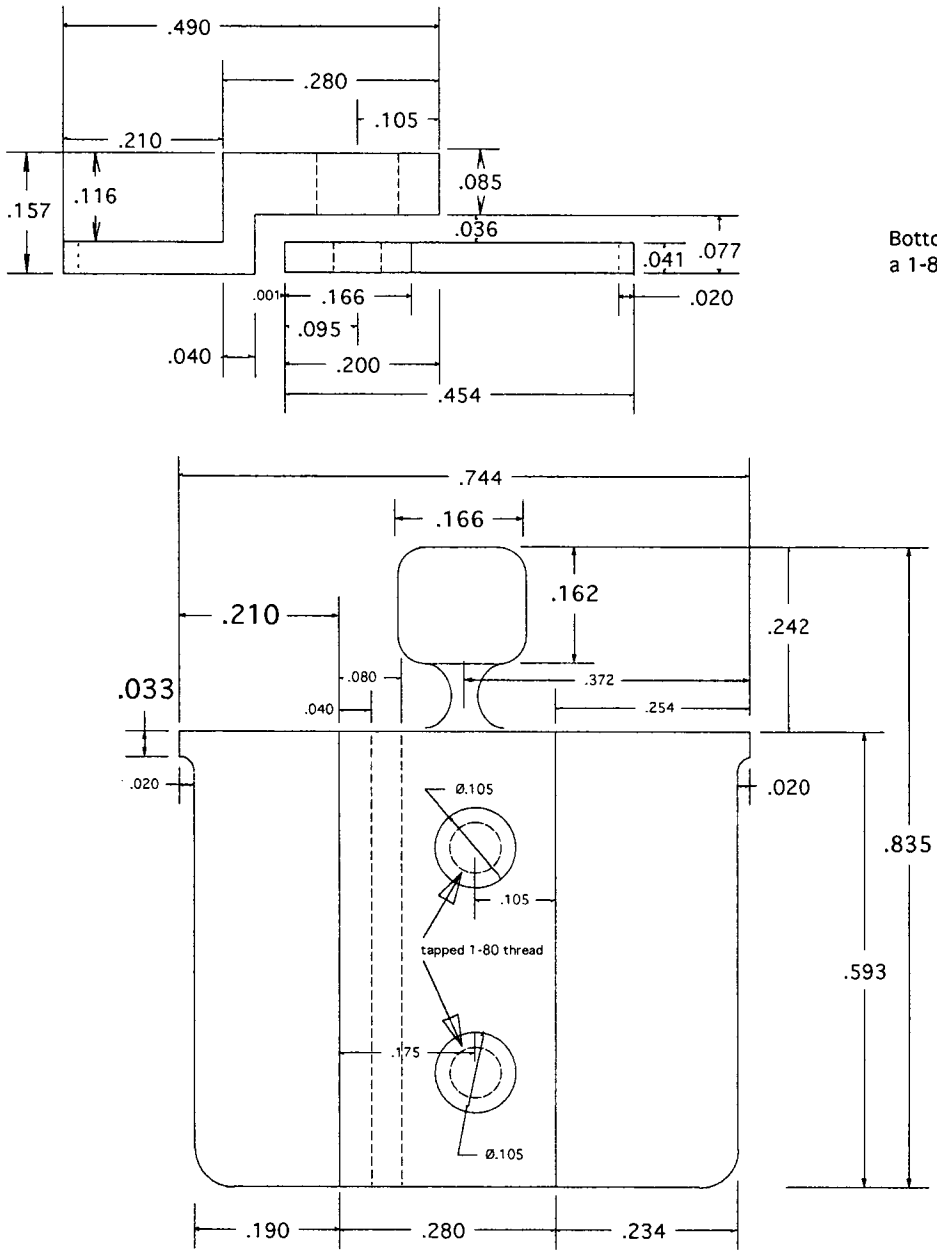

Figure 4.1. CAD drawing of the Si wafer holder. The two halves of the holder are electrically isolated from each other to permit current to flow across the Si sample. Dimensions are in inches. Tantalum wire loops were spot welded to each piece (not shown) and the ends of the wafer were inserted into the loops.

Reproduced with permission of the copyright owner. Further reproduction prohibited without permission.

Arrays of single steps were obtained using the following annealing sequence[6]. Wafers were outgassed for 30 minutes at a temperature just below 650°C so as not to remove the oxide layer. The wafers were then flashed to 1200°C for 10 s to remove the oxide and to diffuse residual surface carbon into the bulk. They were then cooled to 1060°C (where single steps are stable) within 12 s and held at this temperature for 1 min. The most important step is a quench from 1060°C to 850°C in less than 3 s to avoid step bunching and/or step height tripling. Thermal disorder from the quench is removed by holding the wafer at 850°C for 1 min and then slowly cooling the sample (within 30 s) to help preserve long range 7x7 domains and kink-free step edges[6]. During the final stages of the heating procedure the pressure in the UHV chamber was in the low 10^{-10} range. We found that if the final pressure was too high our sample was disordered and showed traces of carbon contamination in AES. The temperature of the wafer was measured using an Ircon Ultimax Plus UX20P[61] portable radiation thermometer with the emissivity set to 0.4.

Auger electron spectroscopy was used to verify the cleanliness of each sample and LEED was used to ensure long range order. An Auger spectra of the sample, before and after cleaning, is shown in Figure 4.3. A visual check was also done to ensure that the sample maintained its colour and reflectivity. Surface roughening on the scale of microns is visible as a haze on the surface of the sample and is caused by traversing the temperature range of 950-1250°C too slowly and at too high a pressure[62,63].

Next, the appropriate Au coverage was deposited while the sample was held at 650°C. Following evaporation, the sample was annealed at 850°C for 2 minutes to ensure long range order. The Au was deposited from a tungsten basket evaporator which was

Reproduced with permission of the copyright owner. Further reproduction prohibited without permission.

Arrays of single steps were obtained using the following annealing sequence[6]. Wafers were outgassed for 30 minutes at a temperature just below 650°C so as not to remove the oxide layer. The wafers were then flashed to 1200°C for 10 s to remove the oxide and to diffuse residual surface carbon into the bulk. They were then cooled to 1060°C (where single steps are stable) within 12 s and held at this temperature for 1 min. The most important step is a quench from 1060°C to 850°C in less than 3 s to avoid step bunching and/or step height tripling. Thermal disorder from the quench is removed by holding the wafer at 850°C for 1 min and then slowly cooling the sample (within 30 s) to help preserve long range 7x7 domains and kink-free step edges[6]. During the final stages of the heating procedure the pressure in the UHV chamber was in the low 10^{-10} range. We found that if the final pressure was too high our sample was disordered and showed traces of carbon contamination in AES. The temperature of the wafer was measured using an Ircon Ultimax Plus UX20P[61] portable radiation thermometer with the emissivity set to 0.4.

Auger electron spectroscopy was used to verify the cleanliness of each sample and LEED was used to ensure long range order. An Auger spectra of the sample, before and after cleaning, is shown in Figure 4.3. A visual check was also done to ensure that the sample maintained its colour and reflectivity. Surface roughening on the scale of microns is visible as a haze on the surface of the sample and is caused by traversing the temperature range of 950-1250°C too slowly and at too high a pressure[62,63].

Next, the appropriate Au coverage was deposited while the sample was held at 650°C. Following evaporation, the sample was annealed at 850°C for 2 minutes to ensure long range order. The Au was deposited from a tungsten basket evaporator which was

Reproduced with permission of the copyright owner. Further reproduction prohibited without permission.

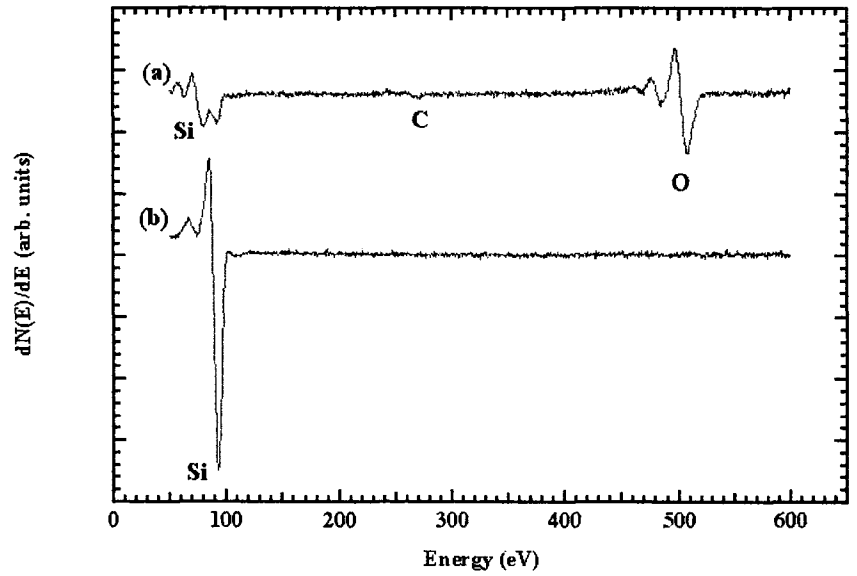

Figure 4.3. Auger spectra of (a) Si with the oxide layer present and (b) clean Si. Notice the absence of the C and O peaks on the clean sample.

calibrated using LEED and AES at a range of coverages on Si(111) miscut 1.1° toward [-1-12][46]. When 0.44 ML of Au is deposited on the Si(111) surface, the surface reconstructs into a 5x2 chain-like pattern[25]. To define the Au coverage we use the density of the Si(111) atomic layer, where 1 ML = 7.8×10^{14} atoms/cm^3. Regions of 5x2 and 7x7 are easily distinguishable in the LEED pattern. Since the 5x2 reconstruction is optimized when 0.44 ML is deposited, correlating the surface reconstruction to Auger peak height ratios is straightforward. Once the evaporator is calibrated, we need only measure the Auger peak height ratios to determine Au coverage on each sample (see Figure 4.4).

The calibration procedure assumes a constant Au flux. This assumption was experimentally verified by comparing Auger peak height ratios for different combinations of evaporation times. For example, the Si/Au peak height ratio for an evaporation time of 4 minutes equals the Si/Au peak height ratio for two evaporations of 2 minutes each (i.e.

Reproduced with permission of the copyright owner. Further reproduction prohibited without permission.

$Si/Au_{4mins}=Si/Au_{2mins+2mins}$). The coverage uncertainty is ± 0.025 ML. Due to the fact that the Au peak is coincident with a minor Si peak, the minimum amount of Au that we can measure with AES is 0.03 ML.

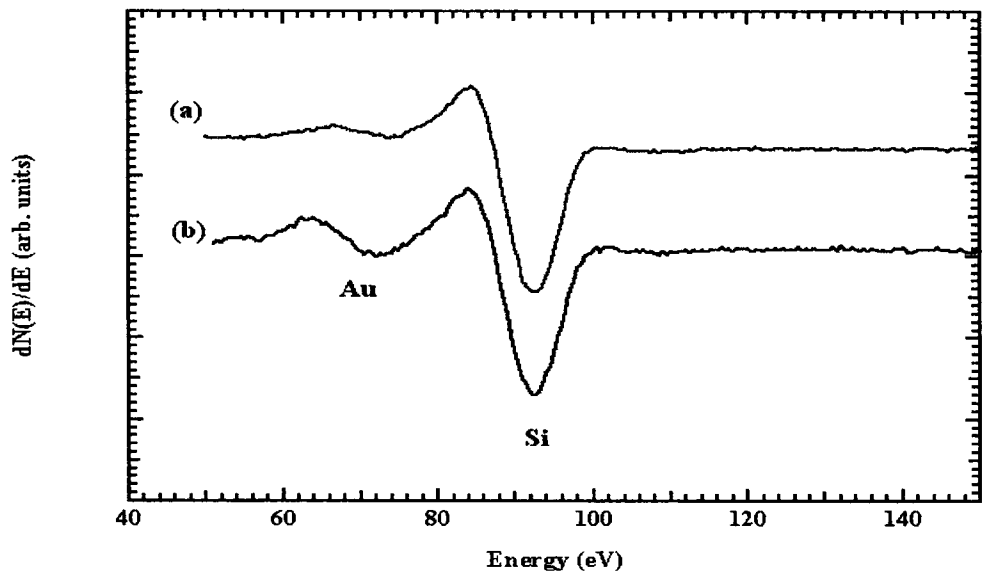

Figure 4.4. Auger spectra (a) clean Si (b) 0.43±0.03 ML Au. Notice that in this spectrum, the Au peak height has increased thereby changing the Si/Au peak height ratios.

Samples were allowed to cool at least 1 hour before STM images were taken to reduce thermal drift. It was possible to study the sample for a period of days by periodically annealing to 830° for a few minutes to remove adsorbed contaminants.

Reproduced with permission of the copyright owner. Further reproduction prohibited without permission.

5. RESULTS AND DISCUSSION

In this thesis, we use a combination of STM and LEED to investigate how submonolayer amounts of Au affect the large scale surface morphology of a vicinal Si wafer miscut from (111) by 8° toward [11-2]. In agreement with previous work[14], we find that depositing submonolayer amounts of Au onto our 8° off-axis wafer produce atomic scale chain-like reconstructions. In addition, we find that submonolayer amounts of Au drastically alter the surface morphology of our 8° off-axis sample in the form of nanofaceting.

We can identify facet orientation using the following formulae to obtain the Miller index (**n**) for a facet[27]:

$$\tan\vartheta = \frac{m}{p} \tag{5.1}$$

$$\mathbf{n} = (p + m, p + m, p - m) \tag{5.2}$$

where ϑ is the angle between the unknown facet and the (111) plane, p is the number of bulk atoms across the terrace and m is the number of single height Si steps separating each terrace. In our case m always equals 1.

We use Figure 5.1, which represents a cut through the bulk Si crystal, to illustrate the relative positions of various facet planes and to help determine p. Any line from the left most point to any other point in Figure 5.1 represents a possible crystal orientation (facet) as labeled by the Miller indices above each point. The points are representative of Si atoms in the bulk crystal. The horizontal line in the middle of the crystal is the (111) plane. Any line below the (111) plane represents a facet tilted toward [11-2] and any line above represents a facet tilted toward [-1-12]. The surface that we are studying is shown as a red line in Figure 5.1. It is characterized by an 8° miscut toward [11-2] where, from

Reproduced with permission of the copyright owner. Further reproduction prohibited without permission.

Figure 5.1, p = 6 and m = 1. Therefore, according to Equation 5.2 the surface corresponds to the (775) plane. In the following discussion, we demonstrate the capability of tailoring the surface morphology simply by varying the Au coverage.

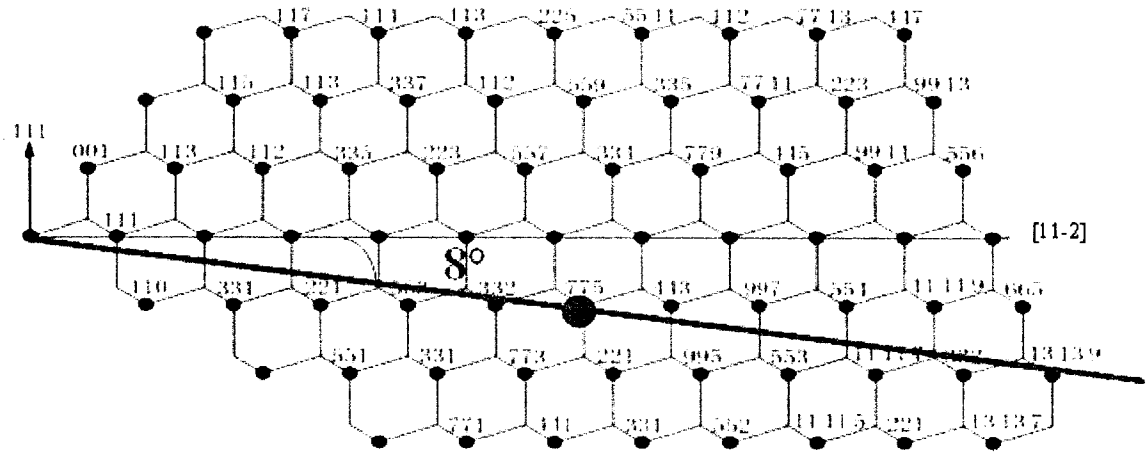

Figure 5.1. The Si Road Map[14] is a representative drawing of a cut through the Si bulk crystal in the (1-10) plane. The dots indicate the position of Si atoms in the bulk and the black horizontal line in the middle of the crystal is the (111) plane. The surface we are studying is shown in red.

All STM images shown in this thesis are typical of what was found in macroscopically separated regions on the same sample. The data were taken at random sampling points from across the sample in constant current imaging mode at room temperature.

Figure 5.2 is an STM image of the clean 8° off-axis sample. We choose to display the image as the derivative of topography, which gives the appearance of a surface illuminated from the left. The derivative of this image, as with all other images presented in derivative mode in this thesis, is rendered using the RHK SPM32 software.

Reproduced with permission of the copyright owner. Further reproduction prohibited without permission.

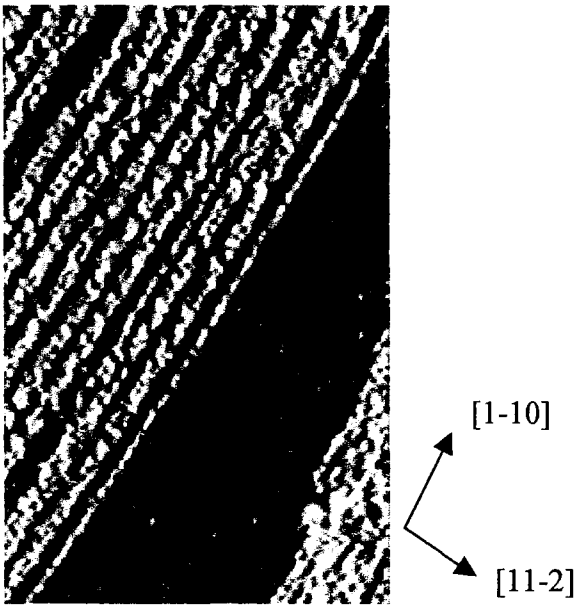

Figure 5.2. STM image (424 Å x 689 Å) of the clean 8° off-axis sample taken at a bias of -2.26 V. The derivative of the topography is shown giving the appearance of a surface illuminated from the left. Si(111) terraces (illuminated regions) are separated by single height steps that cast shadows on the terraces. This array is interupted by regions of step bunching (wide dark areas).

The clean (775) facet is not stable and breaks up into a series of Si(111) terraces (illuminated regions) separated by single height steps. The (111) terraces are 1/2-7x7 unit cells wide (23 Å). Corner holes are barely visible running along each step edge. The array is frequently interrupted by regions of step bunching (wider dark regions). Step bunching is characteristic of samples miscut toward [11-2][64] and it is reported that these regions of step bunching form (331) microfacets[65].

Schwennicke et al.[30] have shown that metal adsorbates on vicinal surfaces profoundly affect step-step interactions. The adsorption of submonolayer amounts of Au induces wholesale restructuring of the surface, stabilizing the (775) surface and eliminating regions of step bunching. Fundamentally, this is why Au adsorption on our off-axis wafer stabilizes the (775) surface. According to previous work by Crain et al.[14], depositing a wide range of Au coverages (0.18-0.32 ML) onto the clean 8° off-axis

Reproduced with permission of the copyright owner. Further reproduction prohibited without permission.

sample results in the (775)-Au reconstruction. Since a particular reconstruction has a specific Au stoichiometry it is unclear where the extra/missing Au atoms are incorporated and, within this range, what the optimal Au coverage is. These authors also report stable (553), (335), (557), (995) and (13 13 7) facets on various off-axis samples at various Au coverages suggesting that the deposition of Au stabilizes a myriad of high index facets[8,14,26]. Contrary to these results, Seehofer et al.[16] report stable (775) facets on 2°, 4° and 9° off-axis wafers at 0.44 ML Au. Similarily, Shibata et al.[15,17] report stable (775) facets on 4° off-axis wafers at 0.7 ML. This suggests that (775) is a low energy facet independent of miscut. In this thesis, we find that the Si(775)-Au facet is stable over a wide range of Au coverages up to 0.32 ML. However, we find that when the coverage is not optimal the large scale surface morphology consists of nanofacets with only portions of the surface exhibiting the (775)-Au reconstruction. In addition, we find that (775)-Au regions are present down to almost zero coverage.

At all Au coverages where we observe (775)-Au termination, STM images of the (775)-Au reconstruction appear identical (allowing for different STM tip conditions) as shown in Figure 5.3. This suggests that the local Au coverage on all (775) facets is always the same. Therefore, the stoichiometry of the (775)-Au surface is constant. In other words, there is always the same number of Au atoms incorporated into the (775)-Au unit cell regardless of the total amount of Au that is deposited on the sample as a whole. As stated above, we find that the Si(775)-Au facet is stable along with nanofacets of various off-axis orientation. The extra/deficit Au must therefore be accommodated by these other nanofacets.

Reproduced with permission of the copyright owner. Further reproduction prohibited without permission.

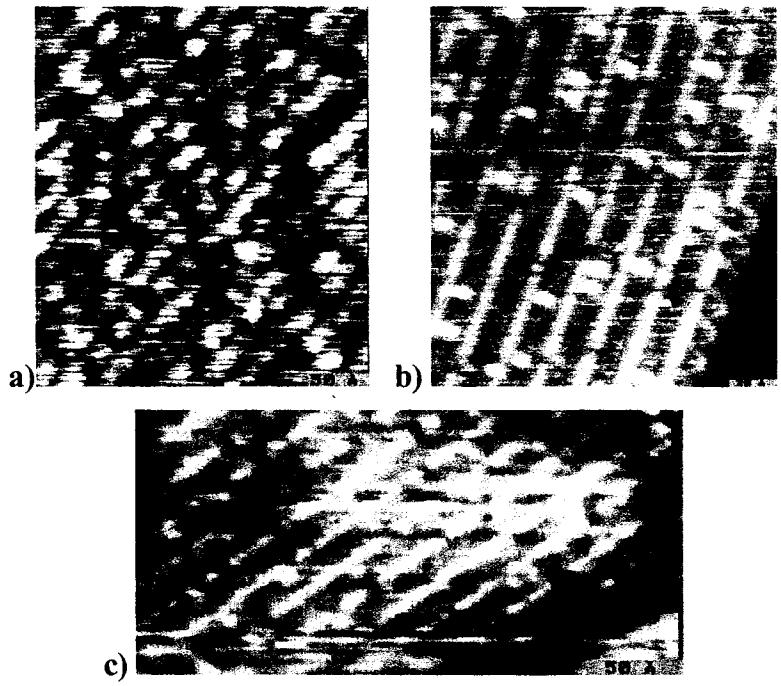

Figure 5.3. Local areas of Si(775)-Au on our 8° miscut sample at various Au coverages: a)0.18 ± 0.03 ML, 280 Å x 280 Å b) 0.24 ± 0.03 ML, 320 Å x 280 Å c) 0.26 ± 0.03 ML, 260 Å x 150 Å. In all images, the chains are spaced 21.3 Å apart and are imaged as protrusions (as are the adatoms). This is characteristic of the (775)-Au reconstruction.

In order to investigate how and where the deficit/extra Au is deposited, we systematically varied the Au coverage and studied the resultant surface morphology using STM and LEED. We define the *low coverage regime* as samples with less than 0.18 ML of Au. In this range, deposition of Au onto the clean 8° off-axis surface and subsequent annealing to 850°C appears to result in wholesale restructuring of the surface. At 0.06 ML of Au, this restructuring includes the formation of (775), (332) and enlarged (111) facets as well as large 3-d structures. It is unclear what the exact nature of the 3-d structures is. Representative data at 0.06 ML Au coverage is shown in Figure 5.4.

The large area STM scan of the surface at 0.06 ML coverage (Figure 5.4a), exhibits flat (775)-Au terminated regions. The flat regions were determined to be (775)-Au by measuring the chain spacing on these areas. The (775)-Au reconstruction is characterized *specifically* by chains spaced 21.3 Å apart.

Reproduced with permission of the copyright owner. Further reproduction prohibited without permission.

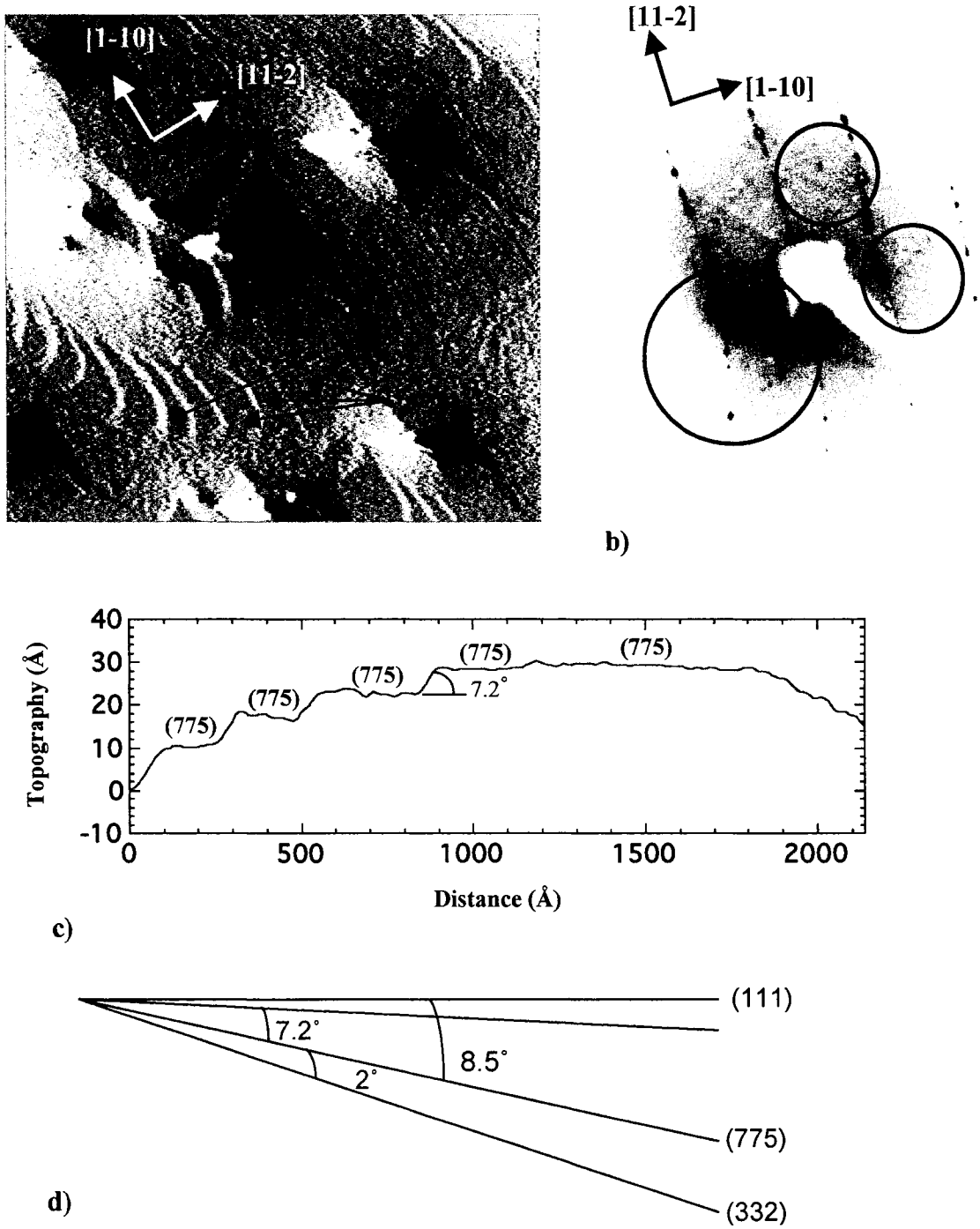

Figure 5.4a) Large scale STM image (5000 Å x 5000 Å) of the clean 8° off-axis wafer with 0.06 ± 0.03 ML Au taken at a bias of 2.19 V. The derivative of topography is shown. The flat terraces are (775)-Au terminated. There are two different facets present, other than (775), in both the step up and step down directions. Large 3-d structures are also present. The black line across the image indicates the position of the line scan. b) Corresponding LEED image (70 eV). The nx2 reconstruction can be seen as rows of spots running along [11-2]. The spot spacing along the rows corresponds to the chain spacing in reciprocal space. Circles indicate the presence of the 7x7 reconstruction that can be seen running diagonally between the rows. c) The line scan shows the relative orientations of the facets. Facet angles were measured to determine the surface structure. Note how, from left to right, they occur in both step up and step down directions. d) Representative drawing of the relative orientations of the facets with respect to the (111) and (775) planes.

Reproduced with permission of the copyright owner. Further reproduction prohibited without permission.

Figure 5.4c is a cross sectional cut through the image (corresponding to the black line across Figure 5.4a) which shows the relative facet angles. This cross section, as well as all others in this thesis, was achieved by first flattening the terraces using the "plane subtract" macro in the SPM 32 software. The angles were then measured using the "section data" macro. It can be seen in Figure 5.4c that, from left to right, there are facets separating the (775) terraces in the step up direction followed by facets in the step down direction. Notice that the step up facets are spaced farther apart than the step down facets. The angle between the step up facets and the (775) plane is, on average, 7.2°. In other words, the facet is 1.3° degrees from the (111) plane. Within experimental uncertainty, this facet is most likely the (111) plane. The angle between the (775) plane and the step down facet is, on average, 2° making the facet 10.5° from the (111) plane. This facet probably corresponds to the (332) plane, which is actually oriented 10.6° from (111) as determined from Figure 5.1 and Equations 5.1 and 5.2. These facets are shown with respect to the (111) plane in Figure 5.4d.

For comparison, at this Au coverage LEED data shows mixed chain-induced and 7x7 reconstructions (see Figure 5.4b). The chain-induced pattern corresponds to the (775)-Au reconstruction. The spacing along the [11-2] direction in the LEED (i.e. in reciprocal space) corresponds to the real space chain spacing. The 7x7 reconstruction is the low energy reconstruction for Si(111) surfaces in the absence of Au. These 7x7 regions are circled in Figure 5.4b. In light of the LEED data, we can assume that at this coverage Au is incorporated into at most two of the three facets (the (775) plane and possibly the (332) facet), leaving at least one face bare and 7x7 terminated. Since the 7x7

Reproduced with permission of the copyright owner. Further reproduction prohibited without permission.

reconstruction occurs on clean (111), this is further evidence that the shallow angle facet in the step up direction is (111).

As noted in the previous section, the minimum amount of deposited Au that we can measure is 0.03 ML. However, even below this threshold LEED indicates the presence of a chain-like reconstruction. The LEED is streaky, but nevertheless quite striking, and suggests that the formation of the Si(775)-Au reconstruction is possible with less than 0.03 ML of Au.

At increasing Au coverage (between 0.18 ML and 0.24 ML), as in Figure 5.5, the LEED ceases to show any traces of the Si(111)7x7 reconstruction. Once again, the surface undergoes drastic restructuring due to the deposition of Au. In STM (Figure 5.5a), there is no indication of both the 3-d structures and facets with angles steeper than (775) (in other words, angles greater than 8.5° from (111)). The absence of facets with steeper off-axis angles suggests that the formation of steep angle facets is linked to the formation of the large 3-d structures. The shallow angle facet present at low Au coverage is now replaced with a facet of increasing off-axis angle as shown in Figure 5.5.

Similar to the low coverage regime, the (775)-Au terminated regions in Figure 5.5a are determined by the chain spacing. As shown in the line scan (Figure 5.5c) the angle between the facets is, on average, 4.1°. From Figure 5.1 and Equations 5.1 and 5.2, this facet corresponds to (13 13 11). There is no evidence that Au is present on the (13 13 11) facet. Overall, we find that the surface preferentially reconstructs to (775)-Au indicating that the (775) facet is energetically favourable. Therefore, as more Au is deposited on the surface, we can assume that more of the surface can become (775)-Au terminated.

Reproduced with permission of the copyright owner. Further reproduction prohibited without permission.

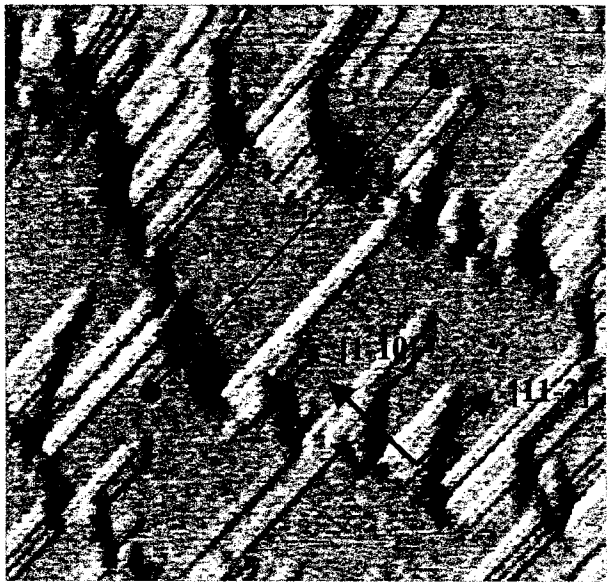

a)

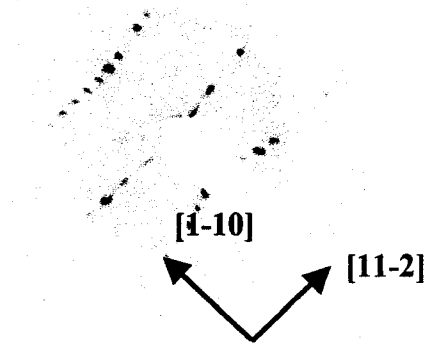

b)

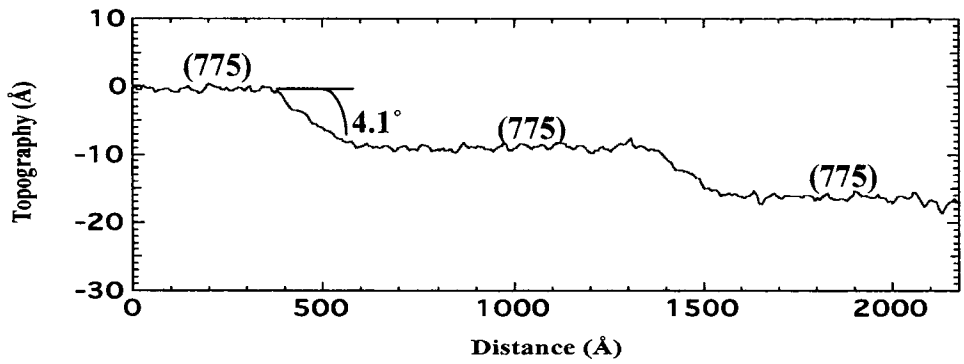

c)

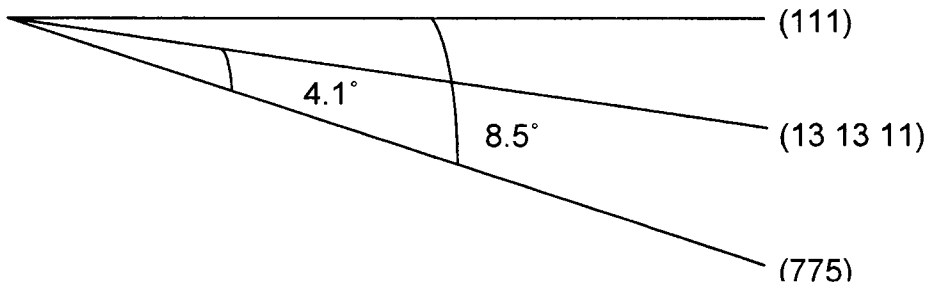

d)

Figure 5.5a) Large area STM image (2500 Å x 2500 Å) of the clean 8° off-axis wafer with 0.20 ± 0.03 ML Au taken at a bias of -2.08 V. The derivative of topography is shown. Again, the addition of small amounts of Au causes large scale surface restructuring. Only the step up direction facet remains, however it is now much closer to the (775) plane than in Figure 5.4a. The line across the image indicates the position of the line scan. b) Corresponding LEED image (70 eV) showing the nx2 reconstruction. There is a pincushion effect as a result of sample position. c) Line scan showing the relative facet angles. d) Representative drawing showing the relative orientation of the facets with respect to the (111) and (775) planes.

Reproduced with permission of the copyright owner. Further reproduction prohibited without permission.

As mentioned in Section 2, the sample must conserve its net angle as well as balance surface stress with the elimination of dangling bonds. Therefore, the change in the surface area of the (775) facet (due to changes in Au coverage) causes a corresponding change in the orientation of the non-(775) facet. We observe a directional trend in this respect as the non-(775) facet progresses from (111)7x7 facet (8.5°) at low coverage toward the (775) direction (i.e. 4.1° at 0.2 ML).

The (775)-Au surface appears to be optimized at a coverage of 0.24 ML. At this coverage, we find that the LEED pattern (Figure 5.6d) is sharp indicating a well ordered surface. There are also 1/2 order streaks running along the [11-2] direction which suggest the presence of a 2x periodicity along the chains. The presence of a streak rather than a spot at the 1/2 order location also indicates a lack of phase correlation between adjacent chains. In other words, the 2x periodicity along each chain is not correlated with the structure on adjacent chains.

As shown in the large scale STM image (Figure 5.6a), 0.24 ML produces regions of (775)-Au (as characterized by the chain spacing) that are large and minimally interrupted by other facets (dark regions). As shown in the corresponding line scan, the angle between (775) and the other facet is small (around 1°). The non-(775) facet is continuing the directional trend of moving toward (775) with increasing Au coverage. This facet corresponds to (443) termination according to Equations 5.1 and 5.2. Note that, ideally the Si(775) surface occurs on a wafer miscut by 8.5°. Since our wafer is miscut by only 8°, these small angle facets are necessary to preserve the total off-axis angle of the wafer.

Reproduced with permission of the copyright owner. Further reproduction prohibited without permission.

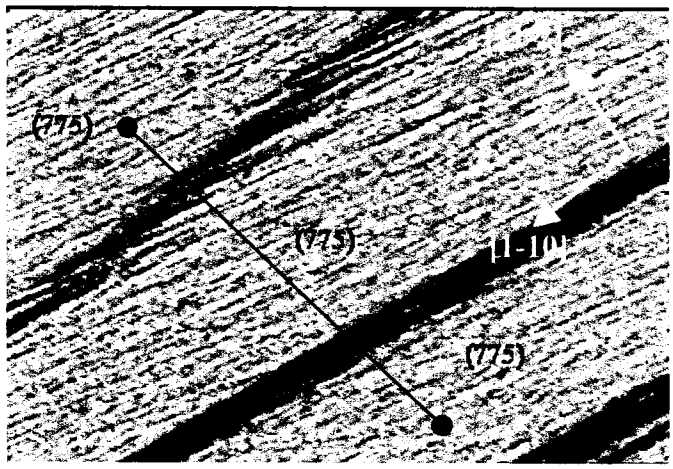

a)

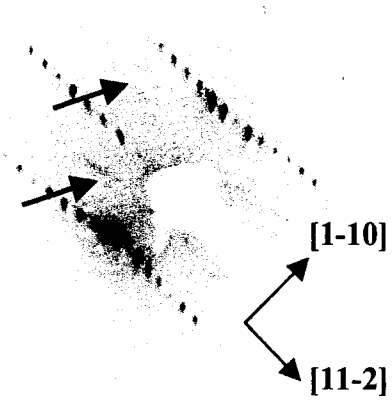

b)

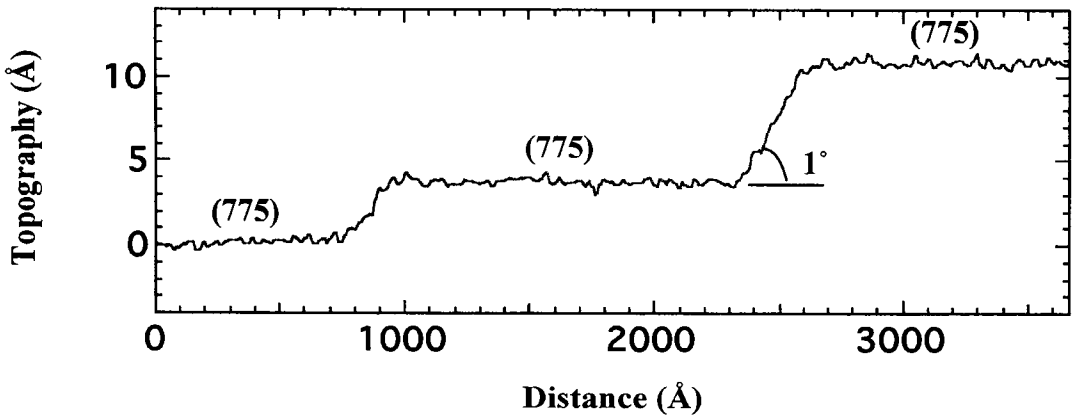

c)

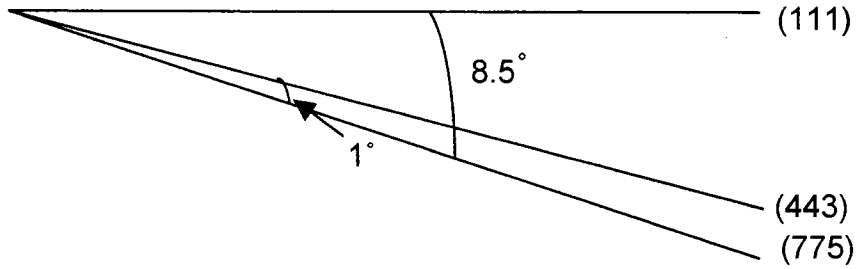

d)

Figure 5.6a) Large scale STM image (4069 Å x 2747 Å) of the clean 8° off-axis wafer with 0.24 ± 0.03 ML taken at a bias of -2.0 V. The derivative of topography is shown. This coverage was determined to optimize the (775)-Au reconstruction. Illuminated terraces are (775)-Au terminated. The line indicates the position of the line scan. b) Corresponding LEED image (70 eV). The arrows show the position of the half-order streaks which suggest a 2x periodicity along the chains. There is a slight pincushion effect due to sample position. c) Line scan showing relative facet angles. The non-(775) facet has moved closer to the (775) plane with increasing Au coverage. d) Drawing depicting the relative facet orientations with respect to the (111) and (775) planes.

Reproduced with permission of the copyright owner. Further reproduction prohibited without permission.

In general, we find that the deposition of 0.24 ± 0.03 ML of Au optimally stabilizes the (775) surface and forms a regular array of chains spaced 21.3 Å apart. Paradoxically, this optimal coverage corresponds to a stoichiometry of 1.5 Au atoms per unit cell. This is highly unusual as previous work[14] suggests that most high index vicinals of Si(111) are stabilized by the incorporation of only one Au atom per unit cell. For comparison, it is also known that the Si(111)5x2-Au reconstruction, which forms on flat (111) surfaces, incorporates two Au atoms in the unit cell[32]. The Si(775)-Au reconstruction appears to be intermediate between these two cases, suggesting a novel surface structure which incorporates elements from both surface reconstructions culminating in one Au atom shared between two unit cells. In this way, 1.5 Au atoms could be attributed to each 1x1 unit cell. Recent work on a similar reconstruction, Si(553)-Au, finds a similar scenario using three-dimensional x-ray diffraction[1]. They find that the unit cell contains two Au atoms; one Au atom having a fixed position within the unit cell and one having split 50-50 occupancy between two almost equivalent sites. In our case, there could be a similar mechanism in the (775)-Au unit cell. However, on average only one of the two additional sites is occupied resulting in a coverage equivalent to 0.24 ML. One extra Au atom every second unit cell may also explain the period doubling observed in LEED.

At coverages beyond optimal (the *over coverage* regime), between 0.24 ML and 0.32 ML, large scale images of the surface again show facets. Representative data for the over coverage regime is shown in Figure 5.7. As shown in Figure 5.7a, at a coverage of 0.26 ML there are two facets present, one of which is (775)-Au terminated as determined by the chain spacing. The angle between the facets, as determined from the line scan in

Reproduced with permission of the copyright owner. Further reproduction prohibited without permission.

Figure 5.7c, is 8.6°. Within error, this facet corresponds to (111) termination, which is 8.5° from (775). Therefore, as the Au coverage increases beyond optimal, the non-(775) facet jumps back toward (111). At this coverage, we observe chains spaced 14 Å apart on the (111) facet indicating the presence of Au (highlighted by arrows in Figure 5.7a). STM also indicates the re-occurrence of 3-d structures, although these are structurally different than those that occurred in the low coverage regime. LEED images at this Au coverage (Figure 5.7b) show an nx2 reconstruction with additional spots along the [11-2] direction. The additional spots indicate the presence of more than one chain spacing. This supports the observation in STM of chains running along the non-(775) facet.

We observe that, as the Au coverage is increased beyond optimal, the (775)-Au reconstruction persists. This suggests that the (775) facet is still energetically preferred in much the same way as in the low coverage regime. However, in the high coverage regime, the non-(775) facet is always observed to be (111)-Au terminated. Thus, excess Au (more than what is stoichiometrically required by the (775)-Au facet) is being accommodated by the (111) facet. This result is in agreement with Seehofer et al. and Shibata et al.[15-17] who observe (775)-Au and (111)5x2-Au facets at various Au coverages. We observe a chain spacing of 14 Å on the (111) facets, which is inconsistent with the (111)5x2-Au chain spacing. Nevertheless, the presence of chains on the (111) terrace is compelling.

As the Au coverage is increased beyond 0.26 ML, the surface structure becomes more difficult to characterize. We observe the formation of triangular shaped terraces at a coverage of 0.32 ML as shown in Figure 5.8.

Reproduced with permission of the copyright owner. Further reproduction prohibited without permission.

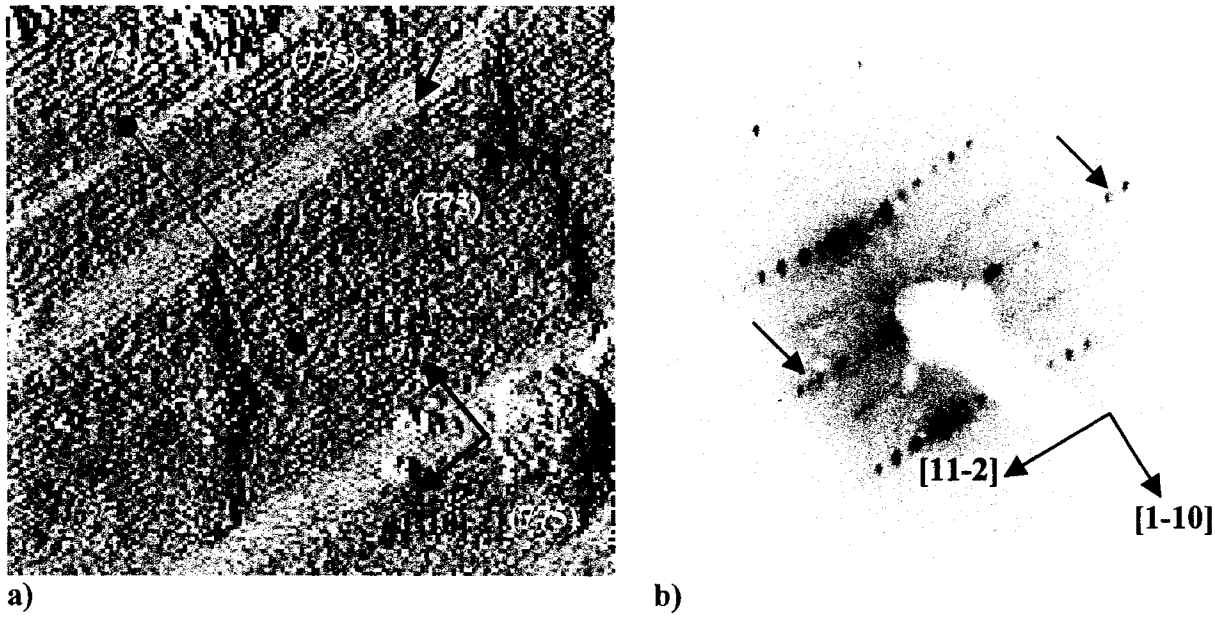

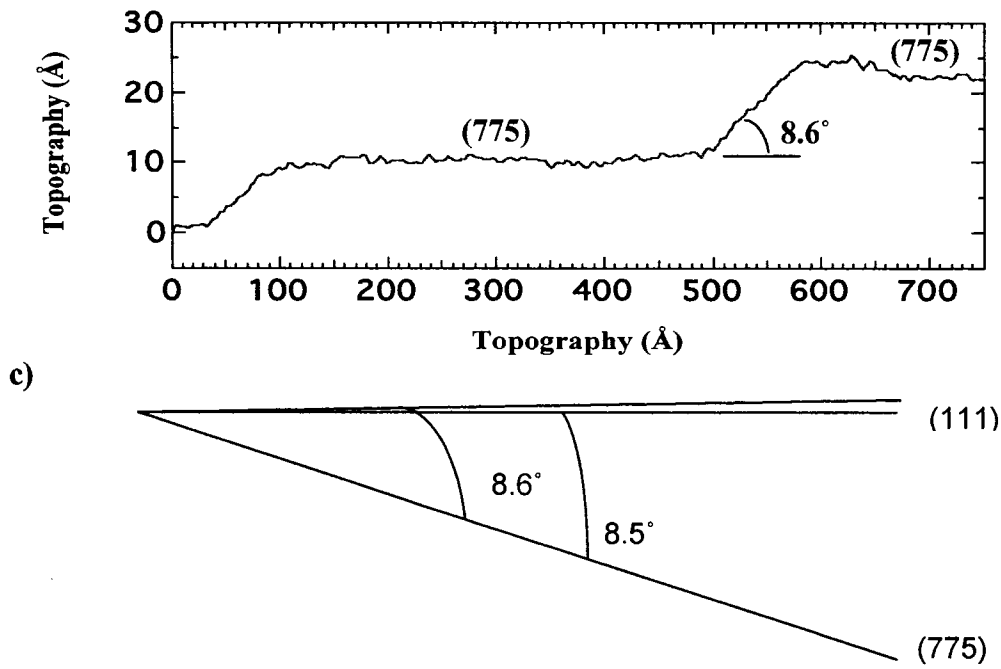

Figure 5.7a) Large scale STM image (1000 Å x 1000 Å) of the clean 8° off-axis wafer with 0.26 ± 0.03 ML Au taken at a bias of -2.04 V. The derivative of topography is shown. As the Au coverage increases beyond optimal, the angle between the two facets increases. Arrows highlight the presence of chains on the non-(775) facet. The line shows the position of the line scan. b) Corresponding LEED image (70 eV). Arrows point to the extra spots which indicate the presence of more than one chain spacing. c) Line scan showing the facet angles. d) Drawing representing the relative facet orientations with respect to (111) and (775) planes.

Reproduced with permission of the copyright owner. Further reproduction prohibited without permission.

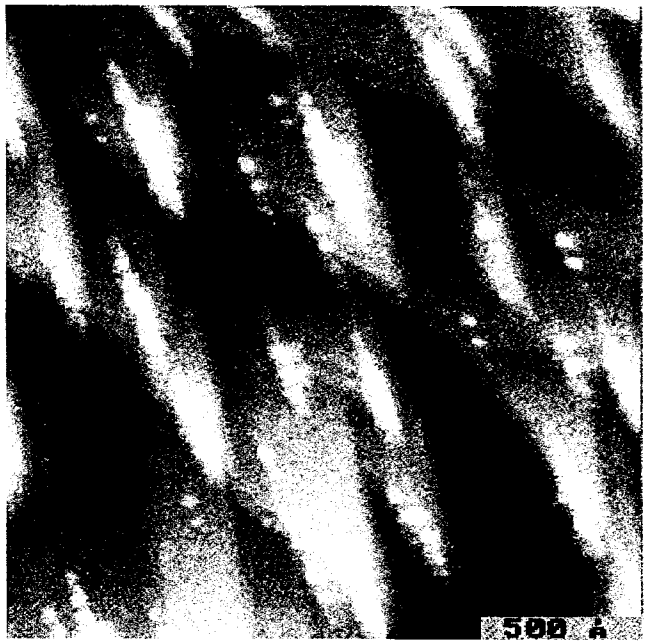

Figure 5.8. Large scale STM image (2000 Å x 2000 Å) of the 8° off-axis wafer with 0.32 ± 0.03 ML Au taken at a bias of 2.05 V. Large triangular shaped terraces dominate the surface structure.

STM shows chains spaced 21.2 Å apart on the triangular shaped terraces indicating the persistence of local (775)-Au termination. LEED images of this surface again show an nx2 reconstruction together with extra spots running along the chains indicating the presence of more than one chain-like reconstruction, although this was not observed in STM.

At approximately 0.32 ML, the (775)-Au surface ceases to be observed in STM, however LEED still shows the presence of a chain-induced reconstruction. One example of this is a 0.43 ML sample shown in Figure 5.9. In Figure 5.9a, the chains are spaced 14.8 Å apart, which corresponds to the (553)-Au reconstruction. Notice that the terrace shape is once again defined by long straight step edges with chains running parallel to the steps, perhaps indicating a local stability in this morphology. The surface exhibits a sawtooth morphology with the angle between the facets being 7.1° (Figure 5.9b).

Reproduced with permission of the copyright owner. Further reproduction prohibited without permission.

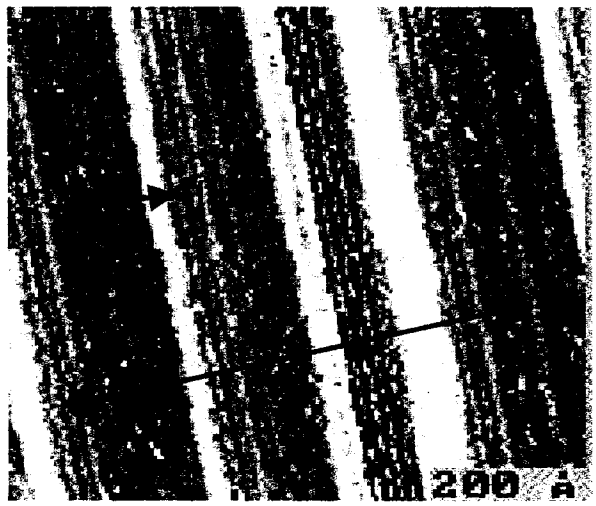

a)

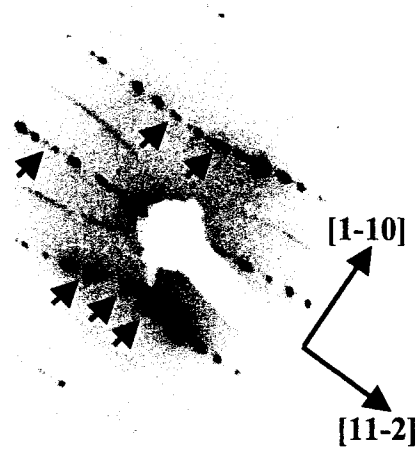

b)

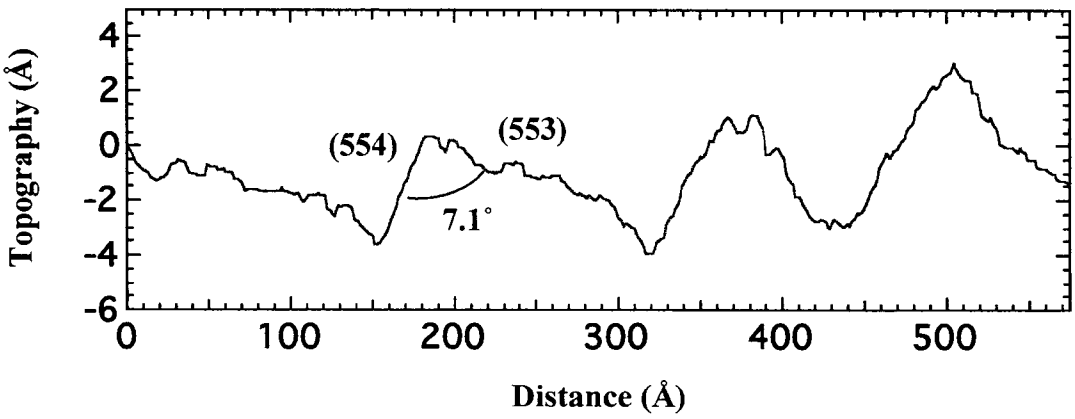

c)

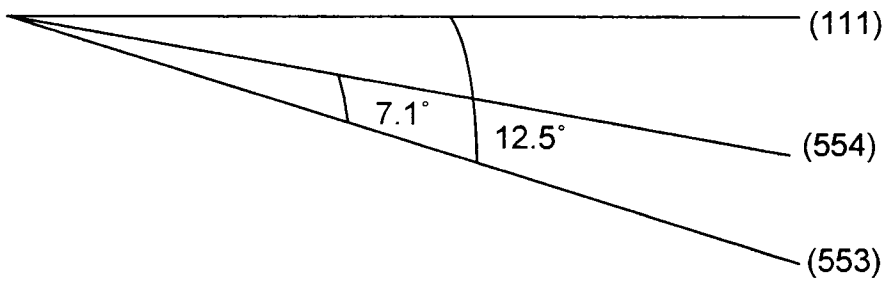

d)

Figure 5.9a) STM image (749 Å x 634 Å) of clean 8° off-axis wafer with 0.43 ± 0.03 ML Au taken at a bias of 2.05 V. At this coverage the (775) facet is not stable and is replaced by (553). The reappearance of long straight facet edges indicates a local stability in the reconstruction. The line indicates the position of the line scan. b) Corresponding LEED image (70 eV). Arrows point at the positions of extra spots indicating the presence of more than one chain spacing. c) Line scan showing relative facet angles. Note the sawtooth morphology. d) Drawing representing relative facet orientations with respect to the (111) plane.

Reproduced with permission of the copyright owner. Further reproduction prohibited without permission.

This corresponds to having both (553) and (554) terminations. There is evidence in Figure 5.9a that there are chains running along the (554) plane as well. LEED (Figure 5.9d) shows a chain-induced reconstruction with extra spots running along the [11-2] direction. This supports STM evidence of the presence of more than one chain-like reconstruction. We also observe (332)-Au termination when just over 0.32 ML of Au is deposited as in Figure 5.10.

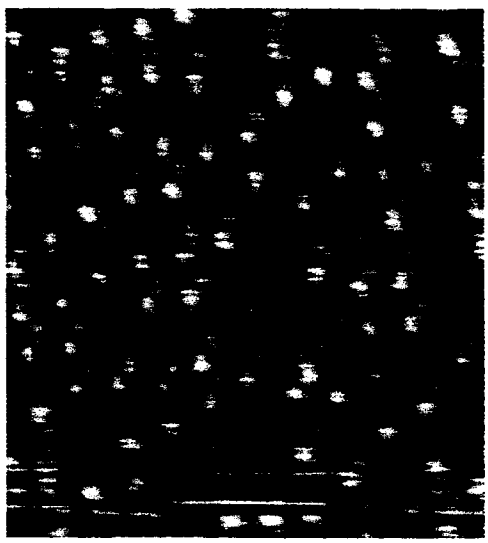

Figure 5.10. Small scale STM image (146 Å x 161 Å) of our clean 8° off-axis wafer with >0.32 ML Au taken at a sample bias of -2.0V. The chain spacing is 17.9Å indicating (332)-Au termination.

The presence of (332) and (553) facets, which replace the (775) facet, could be due to the fact that Au, in far excess of the (775)-Au optimal coverage, can no longer be accommodated by both the (775) and the (111) facets as it was in Figure 5.7. At this coverage, the (775) surface is no longer stable and it is more favourable for the surface to adopt a higher facet angle with a smaller chain spacing. Small chain spacings will incorporate more Au than chains spaced farther apart. Thus, when more than 0.32 ML of Au is deposited, we find that the Si(775) facet is replaced by other terminations with

Reproduced with permission of the copyright owner. Further reproduction prohibited without permission.

smaller chain spacings. Nonetheless, the Si(775)-Au reconstruction persists up to 0.32 ML suggesting that it is a low energy facet.

As mentioned, several authors report the existence of (775)-Au facets on vicinal Si wafers at various Au coverages. Work by Crain et al.[14,26] show that it is possible to achieve stable (775)-Au facets on an 8° off-axis wafer over a range of Au coverages. However, for other miscuts, they show stable (553), (557), (335), (995) and (13 13 7) facets suggesting that the crystallographic orientations nearest to the off-axis angle of the sample are energetically preferred. On the other hand, Seehofer et al. and Shibata et al.[15-17] suggest that the (775) facet is inherently preferred on all vicinal samples. Despite this discrepancy, all of the above mentioned authors agree that (775)-Au is unique in that, unlike its other high index counterparts, it shares many attributes with Si(111)5x2-Au. In Chapter 2 of this thesis, the Si(111)5x2-Au reconstruction was introduced. It normally occurs on flat (111) terraces and is optimized at a Au coverage of 0.44 ML[25], however, it also persists on samples with slight miscuts[66-68]. Crain et al.[14] report similarities in the band structure of Si(775)-Au and Si(111)5x2-Au based on photoemission measurements. Also, the fact that (775)-Au persists over a wide range of Au coverages and sample orientations suggest that it is energetically preferred. This parallels the fact that Si(111)5x2-Au is a low energy reconstruction on the (111) surface[32]. Seehofer et al.[16] note that the (775) terrace (recall from Figure 2.4 that it is a (111) terrace separated by single height steps) is large enough to accommodate a single 5x2 unit cell. Our results suggest that the (775)-Au unit cell is a modified form of the 5x2-Au unit cell to accommodate the highly stepped surface. As well, the stoichiometry of the (775)-Au reconstruction appears to dictate some form of Au sharing. Au sharing may be a property

Reproduced with permission of the copyright owner. Further reproduction prohibited without permission.

required by highly stepped surfaces and the period doubling seen in LEED for nx2 chain-like reconstructions supports this hypothesis. Given that the 5x2-Au reconstruction is energetically preferred on the flat surface, the presence of a highly stepped surface may result in a modified 5x2-Au reconstruction. This would explain the myriad of similarities between the two reconstructions as well as allow for the few differences. It would also explain the inherent tendency for Au-induced surface morphologies to include the (775) facet.

Reproduced with permission of the copyright owner. Further reproduction prohibited without permission.

6. SUMMARY

In this thesis, we have found that the (775)-Au reconstruction persists over a wide range of coverages up to 0.32 ML, and is optimized at a coverage of 0.24 ML. We find that the (775)-Au reconstruction at all coverages appears identical. This suggests that the local Au coverage on all (775)-Au facets is 0.24 ML. The stoichiometry at optimal coverage (0.24 ML) for the (775)-Au reconstruction is such that 1.5 Au atoms are incorporated into each unit cell. We suggest that this stoichiometry can be accomplished though period doubling, and is supported by the presence of half-order streaks in LEED.

When the Au coverage is not optimal, the surface morphology exhibits nanofacets whose orientation depends exquisitely on the Au coverage. Nanofaceting is a result of the balance of surface stress, caused by the conservation of sample angle, with the elimination of dangling bonds[28, 64]. It was observed that extremely small changes in the Au coverage drastically alter the surface structure. Up to 0.32 ML, the (775) facet is always present suggesting that it is energetically preferred. Even at extremely low coverages, < 0.03 ML, the (775)-Au reconstruction is present. As more Au is deposited onto the surface, more of the surface can become (775)-Au terminated. Since the local Au coverage on the (775) facet is 0.24 ML, the deficit/extra Au is accommodated by the non-(775) facet. The change in the surface area of the (775) facets causes a corresponding change in the orientation of the non-(775) facet as defined by Equation 2.1. In the under coverage regime, we see a directional trend in the orientation of the non-(775) facet with increasing Au coverage. A summary of these results is shown in the following phase diagram of surface morphology versus Au coverage.

Reproduced with permission of the copyright owner. Further reproduction prohibited without permission.

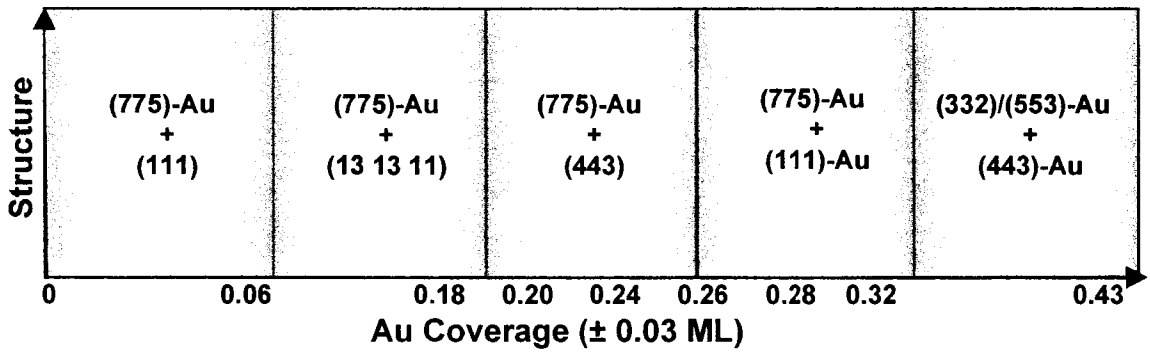

Figure 6.1. Phase diagram of surface structure as a function of Au coverage. Relative facet angles are shown underneath.

In the low coverage regime (up to 0.18 ML), the non-(775) facet does not contain Au. However, in the high coverage regime (0.24 ML – 0.32 ML), we find that the surface morphology is composed of (775)-Au and (111)-Au facets. As the Au coverage is further increased, the surface morphology becomes disordered before reverting to an ordered sawtooth morphology. In this case, at 0.43 ML the (775)-Au reconstruction is no longer present and is replaced by (553)-Au and (554)-Au facets.

Our results show that, up to a threshold of 0.32 ML of Au, the (775) facet is stable. Beyond this threshold, other chain spacings are stabilized. This suggests that, in agreement with Seehofer et al.[16], the (775) facet is indeed energetically preferred. However, in agreement with Crain et al.[14,26], these results also showcase the ability to tune the chain spacing with Au coverage. The discrepancy between these results as alluded to earlier in this thesis is resolved if we attribute the results by Seehofer et al.[16] to the fact that the Au coverage is within the threshold to stabilize the (775)-Au facet. The results by Crain et al.[14] are due to the fact that the (775)-Au threshold has been exceeded. We can verify this hypothesis by repeating our experiment with different off-axis wafers. If the (775) facet is indeed energetically preferred, we expect to find persistent (775)-Au

Reproduced with permission of the copyright owner. Further reproduction prohibited without permission.

facets on any vicinal sample, even on samples miscut further away from the 8.5° miscut required for an ideal (775) facet. To the best of our knowledge, there have been no experiments of this kind to date.

Reproduced with permission of the copyright owner. Further reproduction prohibited without permission.

7. REFERENCES

(1) Ghose, S. K.; Robinson, I. K.; Bennett, P. A.; Himpsel, F. J., Structure of double row quantum wires in Au/Si(553). *Surface Science* **2005,** 581, 199 - 206.

(2) Viernow, J.; Lin, J.-L.; Petrovykh, D. Y.; Leibsle, F. M.; Men, F. K.; Himpsel, F. J., Regular step arrays on silicon. *Applied Physics Letters* **1998,** 72, 948 - 950.

(3) Kirakosian, A.; Lin, J.-L.; Petrovykh, D. Y.; Crain, J. N.; Himpsel, F. J., Functionalization of silicon step arrays I: Au passivation of stepped Si(111) templates. *Journal of Applied Physics* **2001,** 90, 3286 - 3290.

(4) Himpsel, F. J.; Kirakosian, A.; Crain, J. N.; Lin, J.-L.; Petrovykh, D. Y., Self-assembly of one-dimensional nanostructures at silicon surfaces. *Solid State Communications* **2001,** 117, 149 - 157.

(5) Himpsel, F. J.; Altmann, K. N.; Bennewitz, R.; Crain, J. N.; Kirakosian, A.; Lin, J.-L.; McChesney, J. L., One-dimensional electronic states at surfaces. *Journal of Physics: Condensed Matter* **2001,** 13, 11097-11113.

(6) Lin, J.-L.; Petrovykh, D. Y.; Viernow, J.; Men, F. K.; Seo, D. J.; Himpsel, F. J., Formation of regular step arrays on Si(111)7x7. *Journal of Applied Physics* **1998,** 84, 255 - 260.

(7) Crain, J. N.; Kirakosian, A.; Altmann, K. N.; Bromberger, C.; Erwin, S. C.; McChesney, J. L.; Lin, J.-L.; Himpsel, F. J., Fractional Band Filling in an Atomic Chain Structure. *Physical Review Letters* **2003,** 90, 176805.

(8) Altmann, K. N.; Crain, J. N.; Kirakosian, A.; Lin, J.-L.; Petrovykh, D. Y.; Himpsel, F. J., Electronic structure of atomic chains on vicinal Si(111)-Au. *Physical Review B* **2001,** 64, 035406.

(9) Baski, A. A.; Saoud, K. M.; Jones, K. M., 1-D nanostructures grown on the Si(5 5 12) surface. *Applied Surface Science* **2001,** 7150, 1-7.

(10) Losio, R.; Altmann, K. N.; Kirakosian, A.; Lin, J.-L.; Petrovykh, D. Y.; Himpsel, F. J., Band Splitting for Si(557)-Au: Is It Spin-Charge Separation? *Physical Review Letters* **2001,** 86, 4632-4635.

(11) Luttinger, J. M., An exactly soluble model of a many-fermion system. *Journal of Mathematical Physics* **1963,** 4, 1154-1162.

(12) McChesney, J. L.; Crain, J. N.; Perez-Diests, V.; Zheng, F.; Gallagher, M. C.; Bissen, M.; Gundelach, C.; Himpsel, F. J., Electronic stabilization of a 5x4 dopant superlattice on Si(111)5x2-Au. *Physical Review B* **2004,** 70, 195430.

(13) Peierls, R. F., *Quantum Theory of Solids*. ed.; Oxford University Press: London, 1955.

Reproduced with permission of the copyright owner. Further reproduction prohibited without permission.

(14) Crain, J. N.; McChesney, J. L.; Zheng, F.; Gallagher, M. C.; Snijders, P. C.; Bissen, M.; Gundelach, C.; Erwin, S. C.; Himpsel, F. J., Chains of gold atoms with tailored electronic states. *Physical Review B* **2004,** 69, 125401.

(15) Shibata, M.; Sumita, I.; Nakajima, M., Scanning-tunneling-microscopy study of initial stages of Au adsorption on vicinal Si(111) surfaces. *Physical Review B* **1996,** 53, 3856-3860.

(16) Seehofer, L.; Huhs, S.; Falkenberg, G.; Johnson, R. L., Gold-induced facetting of Si(111). *Surface Science* **1995,** 329, 157-166.

(17) Shibata, M.; Sumita, I.; Nakajima, M., Structure and width of Au-adsorbed narrow Si(111) terraces. *Physical Review B* **1998,** 57, 1626-1630.

(18) Tanner, B. K., *Introduction to the Physics of electrons in Solids*. ed.; Cambridge University Press: New York, 1995.

(19) Kittel, C., *Introduction to Solid State Physics*. Seventh Edition ed.; John Wiley and Sons: Toronto, 1996.

(20) Binning, G.; Rohrer, H.; Gerber, C.; Weibel, E., 7x7 Reconstruction on Si(111) Resolved in Real Space. *Physical Review Letters* **1983,** 50, 120-123.

(21) Bartelt, N. C.; Williams, E. D.; Phaneuf, R. J.; Yang, Y.; Sarma, S. D., Orientational stability of silicon surfaces. *Journal of Vacuum Science and Technology A* **1989,** 7, 1898-1905.

(22) Schlier, R. E.; Farnsworth, H. E., Structure and Adsorption Characteristics of Clean Surfaces of Germanium and Silicon. *Journal of Chemical Physics* **1959,** 30, 917-926.

(23) Takayanagi, K.; Tanishiro, Y.; Takahashi, M.; Takahashi, S., Structural analysis of Si(111)-7x7 by UHV-transmission electron diffraction and microscopy. *Journal of Vacuum Science and Technology A* **1985,** 3, 1502.

(24) Stroscio, J. A.; Kaiser, W. J., *Scanning Tunneling Microscopy*. ed.; Academic Press Limited: London, 1993.

(25) Bauer, E., The Si(111)-(5x1) Au structure. *Surface Science* **1991,** 250, L379-L382.

(26) Crain, J. Electronic Structure of 1-dimensional atom chains on silicon surfaces. Department of Physics, PhD. Dissertation, University of Wisconsin-Madison, Madison, 2003.

(27) Chadi, D. J., Theoretical study of the atomic structure of silicon (211), (311), and (331) surfaces. *Physical Review B* **1984,** 29, 785-792.

Reproduced with permission of the copyright owner. Further reproduction prohibited without permission.

(28) Williams, E. D.; Bartelt, N. C., Thermodynamics of Surface Morphology. *Science* **1991,** 251, 393-251.

(29) Dougherty, D. B.; Lyubinetsky, I.; Einstein, T. L.; Williams, E. D., Distinguishing step relaxation mechanisms via pair correlation functions. *Physical Review B* **2004,** 70, 235422.

(30) Schwennicke, C.; Wang, X.-S.; Einstein, T. L.; Williams, E. D., Evolution of surface morphology of vicinal Si(111) surfaces after aluminum deposition. *Surface Science* **1998,** 418, 22-31.

(31) Sanchez-Portal, D.; Martin, R. M., First principles study of the Si(557)-Au surface. *Surface Science* **2003,** 532-353, 655-660.

(32) Erwin, S. C., Self-Doping of Gold Chains on Silicon: A New Structural Model for Si(111)-5x2-Au. *Physical Review Letters* **2003,** 91, 206101.

(33) Kirakosian, A.; Crain, J. N.; Lin, J.-L.; McChesney, J. L.; Petrovykh, D. Y.; Himpsel, F. J.; Bennewitz, R., Silicon adatoms on the Si(111)5x2-Au surface. *Surface Science* **2003,** 532-535, 928-933.

(34) Erwin, S. C.; Weitering, H. H., Theory of the "Honeycomb Chain-channel" Reconstruction of M/Si(111)-(3x1). *Physical Review Letters* **1998,** 81, 2296-2299.

(35) Droppo, D. Observation of Bilayer Growth in the Initial Epitaxy of Pseudomorphic Mg on Mo (001). Department of Physics, MSc. Dissertation, Lakehead University, Thunder Bay, 1999.

(36) BOC Edwards, http://www.bocedwards.com

(37) Varian, Inc., http://www.varianinc.com

(38) SAES Getters, S.p.A, http://www.seasgetters.com

(39) O'Hanlon, J. F., *A User's Guide to Vacuum Technology*. Second Edition ed.; John Wiley and Sons: New York, 1989.

(40) Davisson, C.; Germer, L. H., Diffraction of Electrons by a Crystal of Nickel. *Physical Review* **1927,** 30, 705-740.

(41) Myers, H. P., *Introductory Solid State Physics*. Second ed.; Taylor and Francis: London, 1997.

(42) OCI Vacuum Microengineering, Inc., http://www.ocivm.com

(43) Hove, M. A. V.; Weinberg, W. H.; Chan, C. M., *Low-Energy Electron Diffraction: Experiment, Theory and Surface Structure Determination.* Springer-Verlag: Berlin, 1986.

Reproduced with permission of the copyright owner. Further reproduction prohibited without permission.

(44) Electrim Corporation, http://www/electrim.com

(45) National Instruments Corporation, http://www.ni.com/labview

(46) Toppozini, L. The design, construction and calibration of an evaporator for submonolayer deposition of Au onto the Si(111) surface. Department of Physics, Honours Thesis, Lakehead University, Thunder Bay, 2004.

(47) Woodruff, D. P.; Delchar, T. A., *Modern Techniques of Surface Science - Second Edition*. Cambridge University Press: Great Britain, 1994.

(48) Hedberg, C. L., *Handbook of Auger Electron Spectroscopy*. Third ed.; Physical Electronics, Inc.: Eden Prairie, 1995.

(49) Auger, M. P., *J. de Phys. Radium* **1925,** 6, 205.

(50) Chang, C. C., Auger Electron Spectroscopy. *Surface Science* **1971,** 25, 53-59.

(51) Omicron NanoTechnology GmbH, http://www.omicron.de

(52) MacDairmid, A. Self-Assembly of Dithiol Monolayers on Au (111). Department of Physics, MSc. dissertation, Lakehead University, Thunder Bay, 2001.

(53) Binning, G.; Rohrer, H.; Gerber, C.; Weibel, E., Surface Studies by Scanning Tunneling Microscopy. *Physical Review Letters* **1982,** 49, 57-61.

(54) Beiser, A., *Concepts of Modern Physics*. Fifth Edition ed.; McGraw-Hill, Inc.: New York, 1995.

(55) Tersoff, J.; Hamann, D. R., Theory of the scanning tunneling microscope. *Physical Review B* **1985,** 31, 805 - 813.

(56) Bardeen, J., Tunnelling from a many-particle point of view. *Physical Review Letters* **1961,** 6, 57-59.

(57) Lang, N. D., Theory of Single-Atom Imaging in the Scanning Tunneling Microscope. *Physical Review Letters* **1986,** 56, 1164-1167.

(58) Lang, N. D., Vacuum Tunneling Current from an Adsorbed Atom. *Physical Review Letters* **1985,** 55, 230-233.

(59) RHK Technology, http://www.rhk-tech.com

(60) Virginia Semiconductor, http://www.virginiasemi.com

(61) Ircon, http://www.ircon.com

(62) Swartzentruber, B. S.; Mo, Y.-W.; Webb, M. B.; Lagally, M. G., *Journal of Vacuum Science and Technology A* **1989,** 7, 2901.

Reproduced with permission of the copyright owner. Further reproduction prohibited without permission.

(63) O'Mahony, J. D.; McGilp, J. F.; Leibsle, F. M.; Weightmen, P.; Flipse, C. F. J., Control of terrace width and atomic step distribution on vicinal Si(111) surfaces by thermal processing. *Semiconductor Science and Technology* **1993,** 8, 495-501.

(64) Baski, A. A.; Erwin, S. C.; Whitman, L. J., The structure of silicon surfaces from (001) to (111). *Surface Science* **1997,** 392, 69 - 85.

(65) Hibino, H.; Fukuda, T.; Suzuki, M.; Homma, Y.; Sato, T.; Iwatsuki, M.; Miki, K.; Tokumoto, H., High-temperature scanning-tunneling-microscopy observation of phase transitions and reconstruction on a vicinal Si(111) surface. *Physical Review B* **1993,** 47, 13027 - 13030.

(66) Collins, I. R.; Moran, J. T.; Andrews, P. T.; Cosso, R.; O'Mahony, J. D.; McGilp, J. F.; Margaritondo, G., Angle-resolved photoemission from an unusual quasi-one-dimensional metallic system: a single domain Au-induced 5x2 reconstruction of Si(111). *Surface Science* **1995,** 325, 45-49.

(67) Losio, R.; Altmann, K. N.; Himpsel, F. J., Continuous Transition from Two- to One-Dimensional States in Si(111)-(5x2)-Au. *Physical Review Letters* **2000,** 85, 808 - 811.

(68) Hasegawa, T.; Hosoki, S.; Yagi, K., Stable phase boundaries between the 7x7 and the 5x2 Au structures on a Si(111) surface studied by high-temperature STM. *Surface Science* **1996,** 355, L295-L299.

Reproduced with permission of the copyright owner. Further reproduction prohibited without permission.